

A STUDY OF DIAMOND NANO-PARTICLES

by

RAJARSHI CHAKRABORTY

Presented to the Faculty of the Graduate School of
The University of Texas at Arlington in Partial Fulfillment
of the Requirements
for the Degree of

MASTER OF SCIENCE IN MATERIALS SCIENCE AND ENGINEERING

THE UNIVERSITY OF TEXAS AT ARLINGTON

December 2010

Copyright © by Rajarshi Chakraborty 2010

All Rights Reserved

ACKNOWLEDGEMENTS

It is a pleasure to express my gratitude to the people who made this thesis possible. It is difficult to overstate my gratitude to my advisor, Prof. Suresh C Sharma. With his enthusiasm, his inspiration, and his great efforts to explain things clearly and simply, he helped to spark the research interest in me. Without his fatherly guidance and cooperation this thesis would not have been possible. I would like to thank my colleagues Kyle LaRoque, for his assistance in spectrum analysis, Ajani Ross for his assistance in computation, Alfonso Hinojosa and Kunal Tiwari for their kind assistance with giving wise advice and helping with various applications. I wish to express my warm and sincere thanks to Dr. Ali R Koymen and Dr. Yaowu Hao for agreeing to serve on the thesis committee. I also wish to thank Dr. Efstathios Meletis for his help and guidance. The financial support of the Department of Physics is gratefully acknowledged. I wish to express my thanks to Dr. Muhammed Yousufuddin for his help in using of the instruments related to this research at Center for Nanostructured Materials. The help of Margaret Jackymack will always be remembered. I wish to thank my friends Abhinav Jagetia, Gaurab Dutta and Diya Bhattacharjee for their constructive and valuable suggestions and emotional support. I wish to express my sincere thanks to Prof. Purushottam Chakraborty at Saha Institute of Nuclear Physics, Kolkata, for his guidance throughout my career and my brother Soham Chakraborty for being the strong supportive pillar throughout my life. Lastly, and most importantly, I wish to thank my parents, Dr. Siddhartha Chakraborty and Mrs. Sumita Chakraborty for helping me get through the difficult times, and for all the emotional support and caring they provided. Their ideals and concepts have had a remarkable influence on my entire life.

December 17, 2010

ABSTRACT

A STUDY OF DIAMOND NANOPARTICLES

Rajarshi Chakraborty, M.S.

The University of Texas at Arlington, 2010

Supervising Professor: Suresh C Sharma

Diamond nanoparticles grown previously by Hot Filament Assisted Chemical Vapor Deposition have been characterized by utilizing Atomic Force Microscopy, Scanning Electron Microscopy, Raman Spectroscopy and X Ray Diffraction. AFM and SEM data shows increase in nanoparticle size with growth period ranging from about 20 nm for 15 minutes to 200 nm for 105 minutes growth. Raman spectra have been analyzed by using optical phonon confinement in nanometer size crystals. Based on the SEM, Raman spectroscopy and XRD data, we present clear evidence for nanometer size (10-200 nm) diamond particles in CVD-grown diamond thin films.

TABLE OF CONTENTS

ACKNOWLEDGEMENTS.....	iii
ABSTRACT.....	iv
LIST OF ILLUSTRATIONS.....	vii
LIST OF TABLES.....	x
Chapter	Page
1. INTRODUCTION.....	1
1.1 Diamond – Bulk and Nanoparticles.....	1
1.2 Diamond Nanoparticles.....	2
1.3 Focus of the Thesis.....	3
1.3 Thesis Outline.....	3
2. DIAMOND, GRAPHITE AND DIAMOND POLYMORPHS.....	4
2.1 Natural Diamond.....	4
2.1.1 Diamond Structure.....	5
2.1.2 High Pressure High Temperature Formation.....	5
2.1.3 Chemical Vapor Deposition Growth.....	6
2.1.4 Defects in Diamond.....	6
2.2 Graphite.....	9
2.2.1 Defects in Graphite.....	10
2.3 Hexagonal Diamond.....	11
2.4 Diamond Thin Film.....	12
2.4.1 CVD Growth Process.....	13
3. CHARACTERIZATION TECHNIQUES.....	15
3.1 Introduction.....	15

3.2 Atomic Force Microscopy	15
3.2.1 Imaging Modes	16
3.2.2 Contact Mode	16
3.2.3 Non-Contact Mode	17
3.2.4 Tapping Mode.....	17
3.2.5 Instrument Specifications	18
3.3 Scanning Electron Microscopy	18
3.3.1 Working	19
3.3.2 Resolution.....	20
3.3.3 Wavelength Dispersive X-ray Spectroscopy (WDX)	20
3.3.4 Energy Dispersive X-ray Spectroscopy (EDX).....	20
3.3.5 Back Scattered Electron Imaging (BEI).....	20
3.3.6 Secondary Electron Imaging (SEI).....	21
3.3.6 Instrument Specifications	22
3.4 Raman Spectroscopy	22
3.4.1 Physics of Raman Scattering	23
3.4.2 Mathematical Model of Raman Scattering	25
3.4.3 Phonon Interaction	25
3.5 X- Ray Diffraction	27
3.5.1 Diffraction and Bragg's Law	27
3.5.2 Functions	29
4. RESULTS AND DISCUSSION	30
4.1 Atomic Force Microscopy Results	30
4.1.1 AFM Scan of SH76#1 (15 minutes).....	30
4.1.2 AFM Scan of SH76#2 (30 minutes)	31
4.1.3 AFM Scan of SH76#3 (43 minutes)	32

4.1.4 AFM Scan of SH77#4 (105 minutes)	33
4.2 Scanning Electron Microscopy Results	35
4.2.1 SEM image of SH76#1 (15 minutes)	35
4.2.2 AFM Scan of SH76#2 (30 minutes)	37
4.2.3 AFM Scan of SH76#3 (43 minutes)	38
4.2.4 AFM Scan of SH77#4 (105 minutes)	40
4.2.5 Particle Size Distribution	41
4.2.6 SEM Results of Hexagonal Nanodiamonds	43
4.2.7 Particle Size Distribution of Hexagonal Nanodiamonds	45
4.3 Raman Spectroscopy Results	46
4.3.1 Raman Spectrum of Natural Diamond	47
4.3.2 Raman Results of Samples	47
4.3.3 Concentration Calculations	50
4.3.4 Phonon Confinement	51
4.3.5 Phonon Confinement Model	52
4.3.6 Raman Spectroscopy Results for Hexagonal Nanodiamonds	54
4.4 X-Ray Diffraction Results	56
5. CONCLUSIONS	58
APPENDIX	
RELATIVE DIAMOND CONCENTRATION CALCULATIONS	59
REFERENCES	62
BIOGRAPHICAL INFORMATION	65

LIST OF ILLUSTRATIONS

Figure	Page
2.1 Structure and Bonding in Diamond (a) Structure and (b) Bonding	5
2.2 Carbon Phase Diagrams	6
2.3 Primitive Picture of Nitrogen Vacancy Defects in Diamond.....	8
2.4 Electron Micrograph of (a) Platelets and (b) Octahedral Voids	9
2.5 Structure and Bonding in Graphite (a) Structure and (b) Bonding	10
2.6 Hexagonal Diamond Structure	12
2.7 Block Diagram of CVD Furnace	13
3.1 AFM (a) Working and (b) AFM Tip	16
3.2 Components of SEM	19
3.3 Cu and Al at Different Resolutions (a) SEI-1nA-15mm (b) SEI-1nA-12mm and (c) TOPO-6nA-12mm	21
3.4 Energy Diagram of Raman Effect.....	23
3.5 Vibrational Displacement of A-B about the Equilibrium Position.....	25
3.6 Feynmann Diagrams of Phonon Interaction.....	26
3.7 Diffraction off Crystal Planes	28
4.1 AFM Scan of 15 minutes Sample (a) Top View and (b) Side View	31
4.2 AFM Scan of 30 minutes Sample (a) Top View and (b) Side View.....	32
4.3 AFM Scan of 43 minutes Sample (a) Top View and (b) Side View.....	33
4.4 AFM Scan of 105 minutes Sample (a) Top View and (b) Side View.....	34

4.5 Relative Comparison between the AFM Images of Samples with Growth Period of (a) 15 (b) 30 (c) 43 and (d) 105 min respectively	35
4.6 SEM Micrograph of SH76#1 (15 minutes) – Low Resolution	36
4.7 SEM Micrograph of SH76#1 (15 minutes) – High Resolution	36
4.8 SEM Micrograph of SH76#2 (30 minutes) – Low Resolution	37
4.9 SEM Micrograph of SH76#2 (30 minutes) – High Resolution	38
4.10 SEM Micrograph of SH76#3 (43 minutes) – Low Resolution	39
4.11 SEM Micrograph of SH76#3 (43 minutes) – High Resolution	39
4.12 SEM Micrograph of SH77#4 (105 minutes) – High Resolution	40
4.13 SEM Micrograph of SH77#4 (105 minutes) – Low Resolution	41
4.14 Particle Size Distributions of Diamond Nanoparticles (Clockwise from top left- 15, 30, 43 and 105 minutes)	42
4.15 Crystal Size Vs Growth Time	43
4.16 SEM Micrograph of SH77#4 (a) and (b) High Resolution	44
4.17 SEM Micrograph of SH77#4 – Low Resolution	45
4.18 SEM Micrographs used for Particle Distribution (a), (b) and (c)	46
4.19 Particle Size Distributions of Hexagonal Nanodiamonds	46
4.20 Raman Spectrum of Natural Diamond	47
4.21 Raman Spectra of Samples	48
4.22 Raman Spectra of Samples (Noise Removed)	50
4.23 Relative Diamond Concentration Vs. Growth Time	51
4.24 Crystal size Vs. Time	53
4.25 PCM Fitted to Data	54
4.26 Asymmetric Peak Broadening (Theoretical Calculations)	54
4.27 Raman Spectrum of Hexagonal Nanodiamonds	56
4.28 XRD Results of SH77#4	57

LIST OF TABLES

Table	Page
2.1 Diamond and its Properties	4
2.2 Properties of Hexagonal Diamond.....	11
3.1 Technical Specifications of the Tips used in AFM.....	18
4.1 Size Distribution of Diamond Nanoparticles	43
4.2 Calculated Diamond Concentrations	50
4.3 Calculated Particle Size from PCM	53
4.4 Raman Peaks for SH77#4 (105 minute)	55
4.5 Properties of Cubic and Hexagonal Diamond	57

CHAPTER 1

INTRODUCTION

1.1 Diamond – Bulk and Nanoparticles

Nature provided us with a cornucopia of gemstones which has found their applications in both the cultural heritage and presently in industries and amongst all of them, diamond, probably occupies the pinnacle. The fascination for diamond lies in the fact that apart from its beauty and rarity it has a tremendous potential for diverse applications due to its high thermal conductivity at room temperature, resistance to chemical erosion, extreme hardness, optical transparency etc. The difficulty to exploit these properties due to cost and scarcity led to the necessity of fabricating synthetic diamond in the form of thin films and nanoparticles. It is well known that elements show a change in their properties when confined to nanoscale. The unique mechanical, electrical and optical properties of diamond have imparted special importance for diamond nanoparticles and thin films in recent years where by manipulating matter on an atomic and molecular scale leads to various quantum mechanical effects. An interesting application of diamond thin films are diamond coated tools and surfaces with enhanced hardness. Diamond is non-toxic and biocompatible, hence, an attractive material for biological applications. Nano-diamonds (ND) are emerging as an important material in optics owing to their excellent stability and fluorescence from nitrogen vacancy (N-V) centers [1, 2]. The high-pressure, high-temperature (HPHT) synthesis of diamond is a technique, developed in the 1950s to replicate the conditions (discussed later in chapter 2) under which natural diamonds are formed deep underground. However, the drawbacks like presence of impurities and formation of polycrystalline diamond overrules the chances of applying the process for optical processes. Because of our interest in understanding the properties of diamond, we adopted an alternative clean method of crystal growth i.e., Chemical Vapor Deposition rather than trying to duplicate

nature's method of creating diamond by HPHT. The advantages to CVD diamond growth include the ability to grow diamond over large areas and over a suitable substrate along with the control of the particle size leading to control of the properties. Unlike HPHT, CVD process does not require high pressures and can be achieved easily in the laboratory at low cost.

1.2 Diamond Nanoparticles

Nanodiamonds are nanometer sized diamonds which forms part of the carbon nanomaterial family which, along with fullerenes and nanotubes, has attracted great interest in recent years due to its unique physical and chemical properties. First synthesized in the Soviet Union, commercial production of these nanodiamonds was launched in late eighties of the twentieth century. Detonation nanodiamond is a process of detonating an explosive mixture of Trinitrotoluene (TNT) / cyclotrimethylenetrinitramine (RDX) to form diamond particles of size ~ 5nm [3]. A nanodiamond particle produced by the detonation method is comprised of about 5000 carbon atoms [4]. It is generally accepted that "nano-crystalline" diamond consists of facets less than 100 nm in size, whereas "ultra nano-crystalline diamond" has been coined to describe material with grain sizes less than 10 nm. These differences in morphology originate in the growth process. An alternative mechanism of producing nanodiamonds is Hot Filament Chemical Vapor Deposition where hydrogen and methane gas mixture of high purity is passed through a heated chamber to deposit nanodiamonds on silicon substrate. Due to similarity in the lattices, silicon is chosen as a substrate for diamond film deposition.

Nanodiamonds offer an extraordinary combination of optical, thermal and mechanical properties that, when combined, make it a material that has potential in many advanced applications. Today, a wide range of synthetic and natural diamond products and grades exist, covering medical, industrial, research, telecommunications, data storage and military applications. Diamond electrodes may find applications in analysis of contaminants such as nitrates in water supplies and removal of those contaminants. Diamond fibers and wires have

been fabricated which show exceptional stiffness for their weight. They may find uses as reinforcing agents in metal-matrix composites allowing stronger, stiffer and lighter load-bearing structures. Nanodiamonds can be used as high-performance UV detectors [5].

1.3 Focus of the thesis

This thesis focuses on the study of the properties of nanodiamonds. The nanodiamonds which were previously grown [6,7] were characterized using conventional techniques of Atomic Force Microscopy (AFM), Scanning Electron Microscopy (SEM) , X Ray Diffraction (XRD) and Raman Spectroscopy. AFM was used to study the topography of the nanodiamond samples followed by SEM to analyze the morphology and structure. XRD was used to study the crystal structure of nanodiamonds. Raman spectroscopy was applied to study the confinement of phonons in nanodiamonds and also to understand the particle size distribution of the nanodiamonds.

1.4 Thesis Outline

This thesis is divided into five chapters with the first chapter discussing the basic properties, applications and the necessity for choosing diamond as an optical material. The methods of producing diamond nanoparticles and thin films are also discussed in brief. In the second chapter, an understanding of the structure and properties of diamond and its allotropes are reviewed. The various defects associated with diamond are also highlighted. The third chapter discusses the instruments we have used for characterizing diamond nanoparticles. A description of Atomic Force Microscopy (AFM), Scanning Electron Microscopy (SEM), Raman Spectroscopy and X Ray Diffraction (XRD) is provided. In the fourth chapter we discuss the results obtained from the experiments performed on the diamond nanoparticles followed by the conclusions of the thesis in the final chapter.

CHAPTER 2

DIAMOND AND ITS POLYMORPHS

2.1 Natural Diamond

Diamond is a rare, naturally occurring mineral composed of carbon where each carbon atom in a diamond is surrounded by four other carbon atoms and connected to them by strong covalent bonds. It is one of the hardest naturally occurring mineral known to us. Though initially sought for its ornamental qualities its material characteristics have created greater demand in industry. Diamonds are normally clear or white but some natural diamonds may vary in color varying from yellow to blue. The optical transparency of diamonds has generated uses in optical and electronic devices. Diamond is considered to be one of the best insulators with a band gap of 5.45 eV.

Table 2.1 Diamond and its Properties [8]

Properties	Values
Hardness (kg/mm ²)	10 ⁴
Refractive Index	2.4
Melting Point (°C)	~ 3800
Lattice Constant (Å)	3.567
Band gap (eV)	5.45
Electron mobility (cm ² /V-s)	1900
Hole mobility (cm ² /V-s)	1600

2.1.1 Diamond Structure

Diamond is an allotrope of carbon with each carbon atom surrounded by four other carbon atoms arranged in the corner of a tetrahedron forming face centered cubic (fcc) packing as shown in the Figure 2.1(a) below. Within diamond, one s-orbital and three p-orbitals undergo sp^3 hybridization. The geometry of the hybridized orbital is tetrahedral. This is the reason why each carbon atom within diamond has four nearest neighbors. The bonding is illustrated in Figure 2.1(b). All the electrons of each carbon atom are shared and the octet rule is satisfied. Hence no free electron is left for the conductance of electricity rendering diamond to be a poor electrical conductor at bulk state.

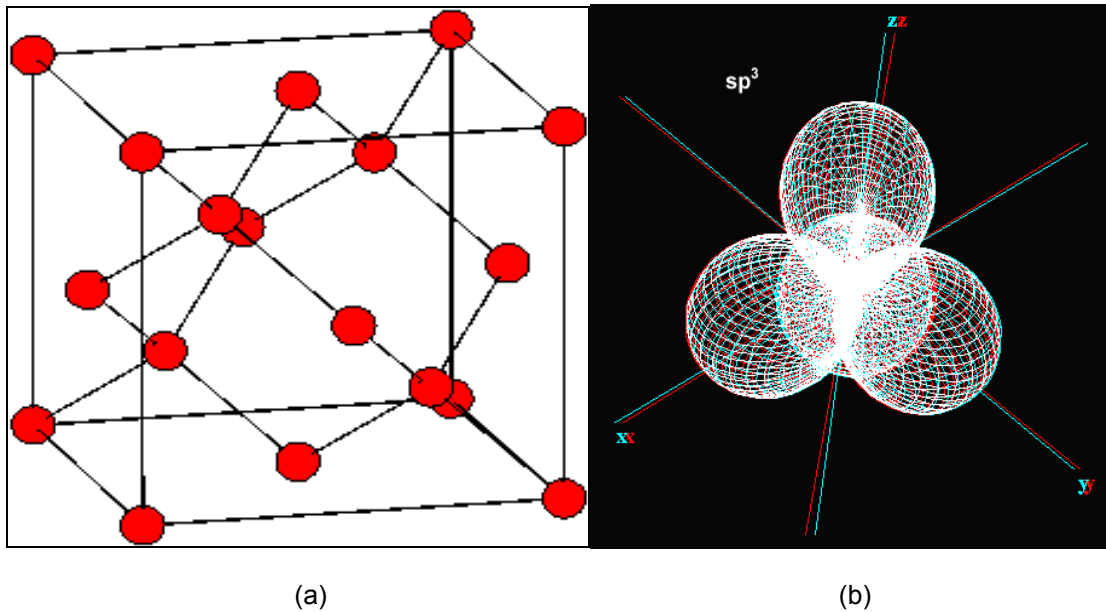


Figure 2.1 Structure and Bonding in Diamond
(a) Structure [9] and (b) Bonding [10]

2.1.2 High Pressure High Temperature Formation

Diamond formation in nature is accompanied by High Pressure High Temperature (HPHT) process where a pressure > 120 kbar and temperature $> 1300^\circ$ C creates diamond from graphite. The HPHT processes can be divided into two main groups of direct and indirect conversions. In direct conversion processes, only carbon and high temperature and high

pressure is needed to produce diamond. In case of indirect conversions, carbon along with other catalysts, solvents etc are used to produce diamond. A phase diagram of carbon is shown in Figure 2.2 to understand the pressure temperature equilibrium of carbon.

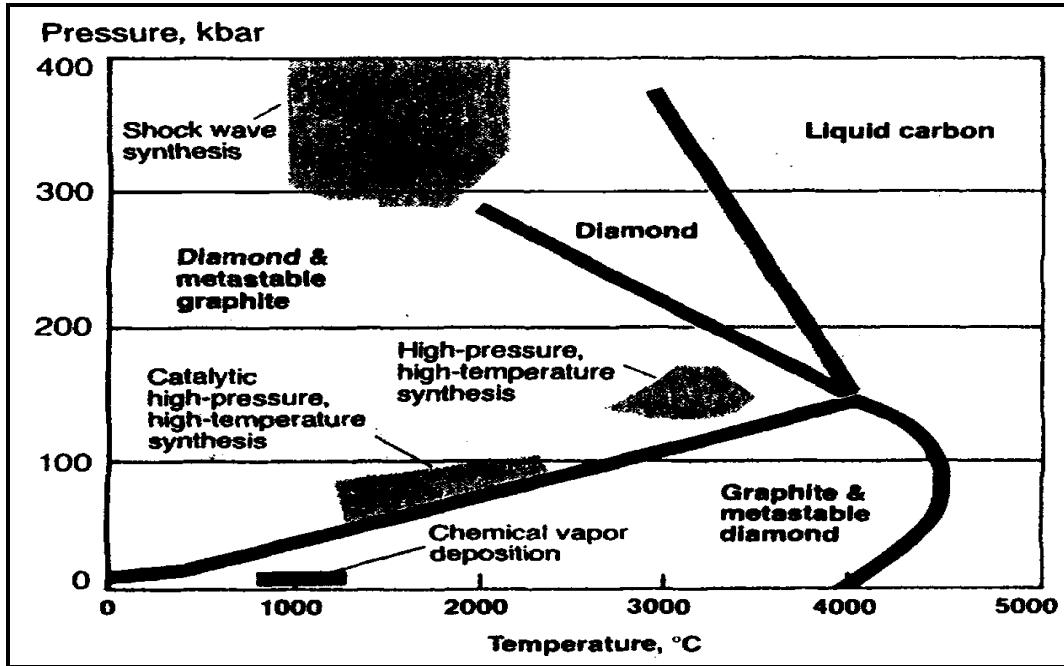


Figure 2.2 Carbon Phase Diagrams [11]

2.1.3 Chemical Vapor Deposition Growth

Our interest in understanding the properties of diamond forced us to follow an alternative clean method of crystal growth i.e., Chemical Vapor Deposition rather than trying to duplicate nature's method of creating diamond by HPHT. The advantages to CVD diamond growth include the ability to grow diamond over large areas and over a suitable substrate along with the control of the particle size leading to control of the properties. Unlike HPHT, CVD process does not require high pressures and can be achieved easily in the laboratory at low cost. Chemical vapor deposition is an outstanding tool for growing diamond from a hydrocarbon gas mixture. This method has been the subject of intensive worldwide research since the early 80s having the primary advantages of growing diamond over large areas, the ability to grow diamond on a

substrate, and the control over the properties of the diamond produced. High pressure high temperature technique produces typically free standing diamond of varying sizes whereas CVD diamond large areas can be coated with diamond.

2.1.4 Defects in Diamond

Nitrogen is a major impurity in diamond which is responsible for many differences in the absorption spectra of diamond. The four main nitrogen forms are C-nitrogen center, A-nitrogen center, B-nitrogen center and N3 nitrogen center. The C center corresponds to electrically neutral single substitutional nitrogen atoms in the diamond lattice. The A center consists of a neutral nearest-neighbor pair of nitrogen atoms substituting for the carbon atoms. B center consists of a carbon vacancy surrounded by four nitrogen atoms substituting for carbon atoms. The N3 center consists of three nitrogen atoms surrounding a vacancy.

The impurities which occupy substitutional positions are nitrogen and boron [12, 13] and are of specific interest since they can alter the electrical properties of diamond. Boron is an acceptor in diamond where each boron atom substituting for a carbon atom creates a hole in the band gap that can accept an electron from the valence band. Due to the small energy (0.37 eV) [14] needed for excitation, holes can be thermally released from the boron atoms to the valence band even at room temperatures. These holes can move in an electric field and render the diamond a p-type semiconductor. Silicon is a common impurity in diamond films grown by chemical vapor deposition and it originates primarily from silicon substrate. Silicon is identified as Si-vacancy complex and acts as a deep donor having an ionization energy of 2 eV, and thus again is unsuitable for electronic applications [15].

Nickel and cobalt traces are also observed in some high-pressure high-temperature grown diamonds.

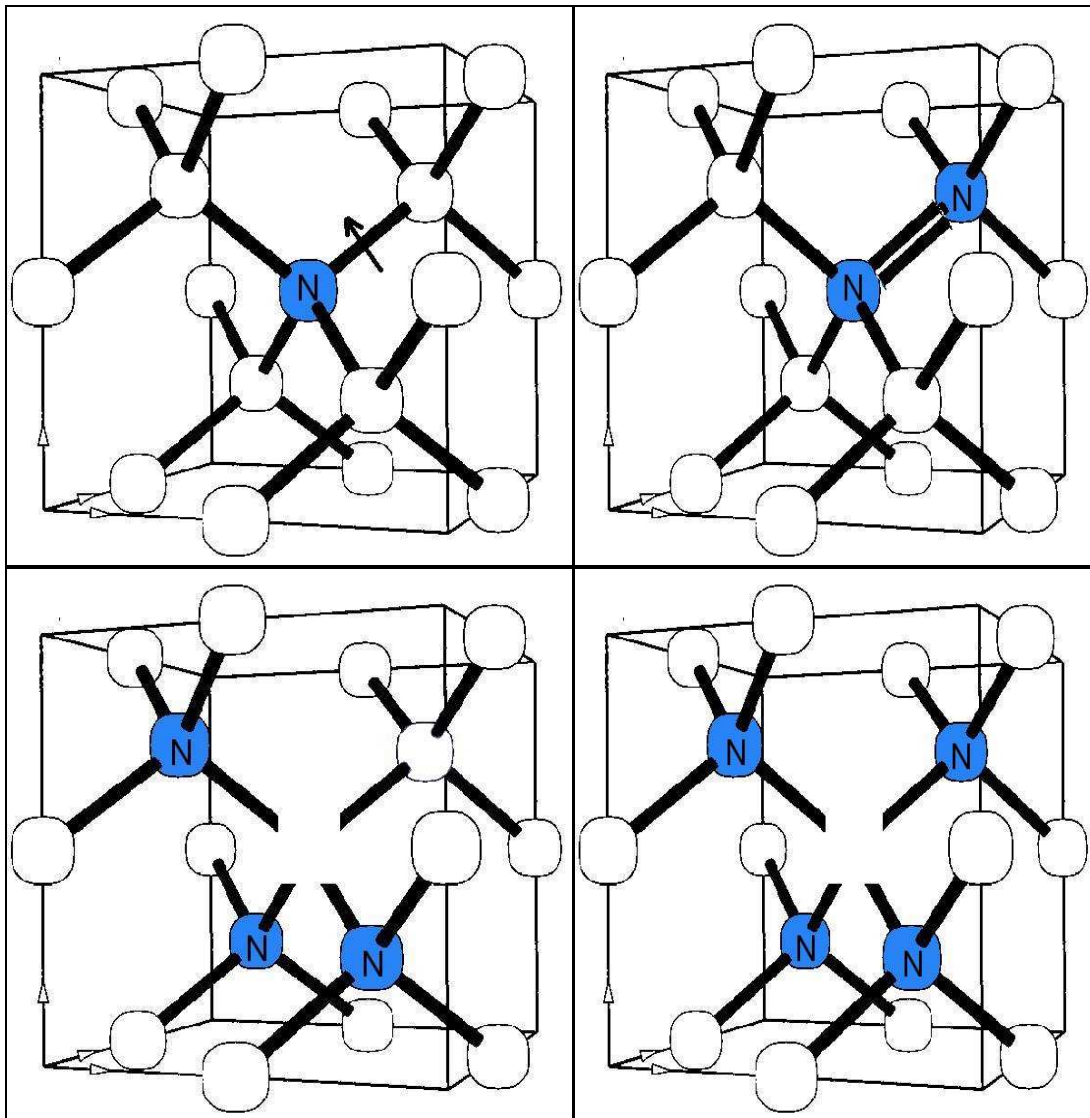


Figure 2.3 [16] Primitive Picture of Nitrogen Vacancy Defects in Diamond

Surface and volume defects include stacking faults, low angle grain boundaries, twin boundaries and hetero-boundaries. The volume defects common in diamond are platelets or inclusions. These are planar defects in the $\langle 100 \rangle$ planes and are a large regular array of carbon interstitials [17]. Voidites are octahedral nanometer-sized clusters present in many natural diamonds, as revealed by electron microscopy [18] and are a result of thermal degradation of platelets.

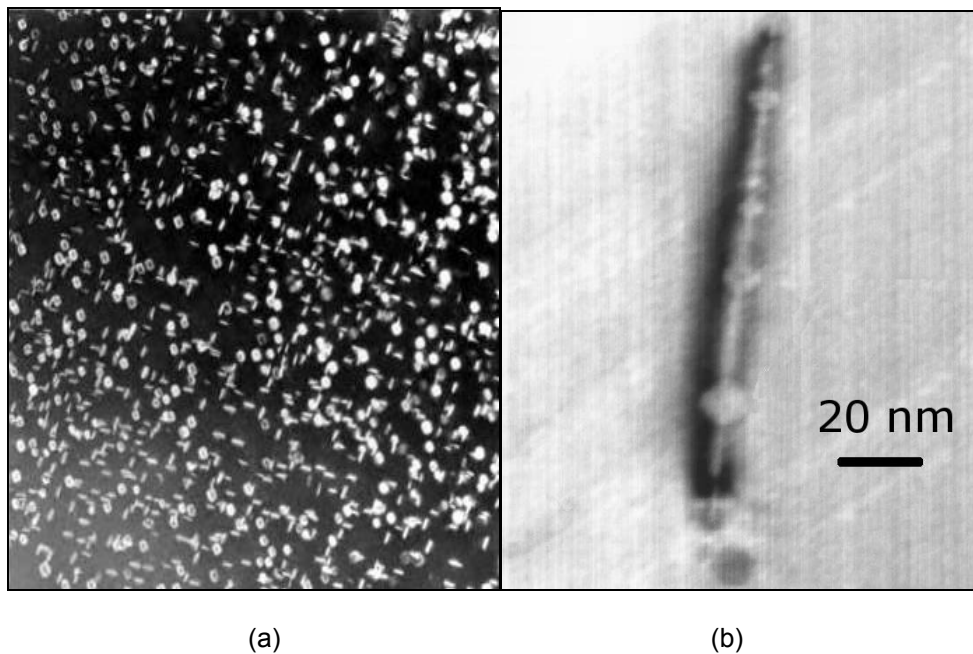


Figure 2.4 Electron Micrograph of (a) Platelets and (b) Octahedral Voids [18]

2.2 Graphite

Graphite is a polymorph of carbon consisting of layers of carbon atoms. In each layer, the carbon atoms are arranged in a hexagonal lattice with separation of 0.142 nm, and the distance between planes is 0.335 nm [20]. The C-C bonds are created from the overlap of two sp^2 hybrid orbitals. Within graphite, one s-orbital and two p-orbitals undergo sp^2 hybridization. The geometry of the hybridized orbital is trigonal planar. This is the reason why each carbon atom within graphite has three nearest neighbors within the graphite sheets. One of the p-orbitals is left unaffected. This last p-orbital overlaps with those from neighboring carbon atoms, in a sideways manner, to form the distributed pi-bonds that reside above and below each graphite sheet. Graphite occurs in two distinct forms, alpha (hexagonal) and beta (rhombohedral). Hexagonal graphite is a thermodynamically stable form of graphite with an ABABAB stacking sequence. Rhombohedral graphite is a thermodynamically unstable allotropic form of graphite with an ABCABC stacking sequence of the layers. High grade amorphous and crystalline

graphite having colloidal property are used as lubricants due to extraordinarily low friction coefficient. Nowadays artificially prepared graphite has replaced natural graphite to a great extent for making furnace electrodes and for modes in the manufacture of chlorine and caustic soda.

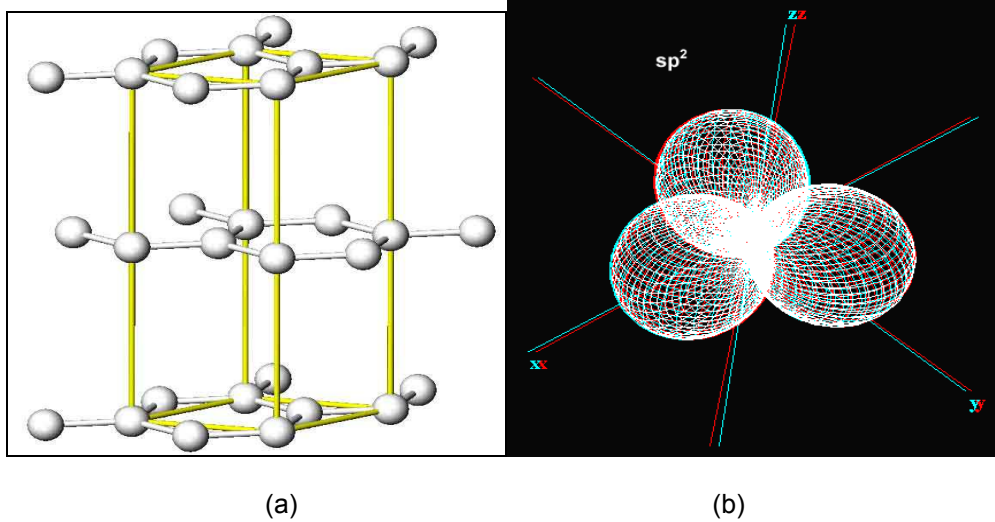


Figure 2.5 Structure and Bonding in Graphite (a) Structure [21] and (b) Bonding [10]

2.2.1 Defects in Graphite

Surface and bulk (structural) defects in graphite play an essential role in many processes involving this material. They influence physical (electronic and thermal conductivity, electronic structure) and chemical (reactivity, activation of adsorbed molecules) properties of graphite. In ideal graphite the hexagonal structure layer extends to infinity. This structure is referred to as a carbon macromolecule. However, vacancies or defects are observed in the structure where impurities like H or a group like OH bond to the defects. The foreign impurities can cause the macromolecule to buckle due to Van der Waal's repulsion envelope around the atom. Graphite also exhibits twinning. Defects in graphite can be due to radiation damage or ion beam implantation.

2.3 Hexagonal Diamond

The probability of existence of hexagonal form of diamond which is also known as Lonsdaleite was first suggested by Lonsdale [22] in 1944 with research still actively being pursued to grow hexagonal diamond. The first report of the formation of hexagonal diamond by transforming crystalline graphite at high pressure and temperature was first reported by Bundy and Kasper[20] in 1967. The C-C bonding in hexagonal structures is sp^3 , with ABABAB stacking sequence. The rare chances of getting hexagonal diamond are explained by the stability and formation conditions. The energetically unfavorable structure makes it rare compared to the cubic phase of diamond. Static pressure along c axis of single crystal hexagonal graphite at room temperatures gives hexagonal diamond. The main reason for the formation of such structures is mechanical twinning due to shock compression. High temperature and stress can transform graphite into diamond, but retains graphite's hexagonal crystal lattice. It is translucent, brownish-yellow in color, and has an index of refraction of 2.40 to 2.41, a specific gravity of 3.2 to 3.3 [23]. Lonsdaleite is simulated to be 58% harder than diamond [24] on the <100> face and to resist indentation pressures of 152 GPa, whereas diamond would break at 97 GPa.

Table 2.2 Properties of Hexagonal Diamond

Properties	Hexagonal Diamond
Structure	Wurtzite
Stacking	ABABAB
Bandgap	4.5eV [25]
Bond length	$a = 2.52\text{\AA}$ and $c = 4.12\text{\AA}$

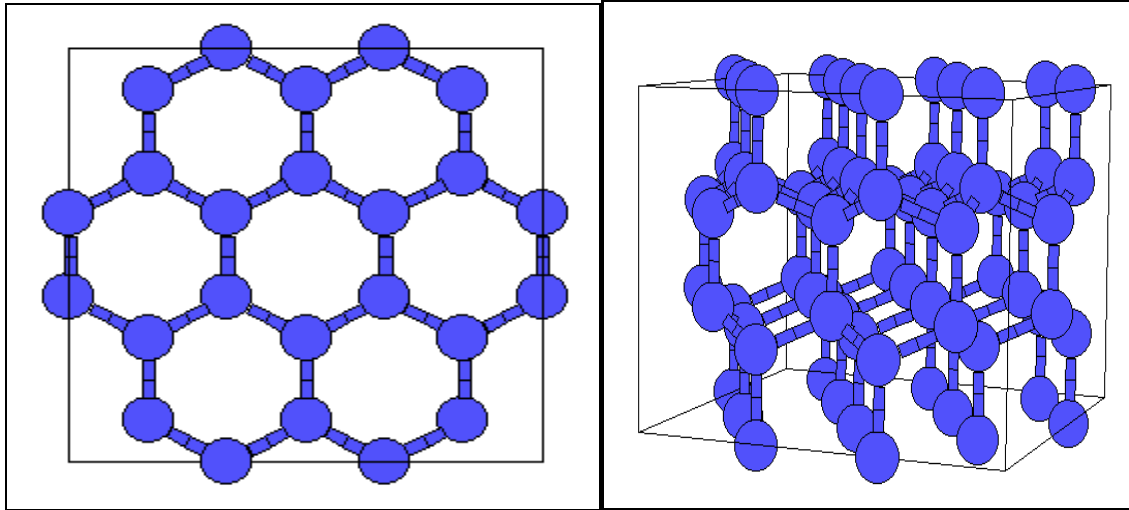


Figure 2.6 Hexagonal Diamond Structure [26]

2.4 Diamond Thin Film

Detonation nanodiamond (DND) is diamond that originates from a detonation of an explosive mixture of TNT/RDX. This method generally yields ultra-disperse diamonds in the range of 50Å [27]. It is one of the easiest methods of producing nanodiamonds with applications ranging from lapping and polishing, additives to engine oils (e.g. ADDO), dry lubricants for metal industry, reinforcing fillers for plastics and rubbers etc. The major difficulty of the process lies in handling and laboratory controlled production in addition to purification. The use of TNT/RDX is hazardous and can be unsafe for laboratory use. The detonation nanodiamond grains mostly have diamond cubic lattice and are structurally imperfect. TNT/RDX explosive mixture – being rich in nitrogen, concentration of pure defect free diamond is low.

Chemical vapor deposition is an outstanding tool for growing diamond from a hydrocarbon gas mixture. This method has been the subject of intensive worldwide research since the early 80s having the primary advantages of growing diamond over large areas, the ability to grow diamond on a substrate, and the control over the properties of the diamond produced. High

pressure high temperature technique produces typically free standing diamond of varying sizes whereas CVD diamond large areas can be coated with diamond.

2.4.1 CVD Growth Process

Figure 2.7 shows the block diagram of the CVD reactor used by others [6, 7, and 38] to grow diamond thin film. The complex chemical and physical processes which occur during diamond CVD starts when process gases first mix in the chamber and pass through an activation region (e.g. a hot filament or electric discharge), which provides energy to the gaseous species. This activation causes molecules to fragment into reactive radicals and atoms, creating ions and electrons, and heats the gas up to temperatures approaching a few thousand Kelvin. Beyond the activation region the reactive components mix and react with the substrate forming diamond. There is also a possibility of desorbing back to gaseous state.

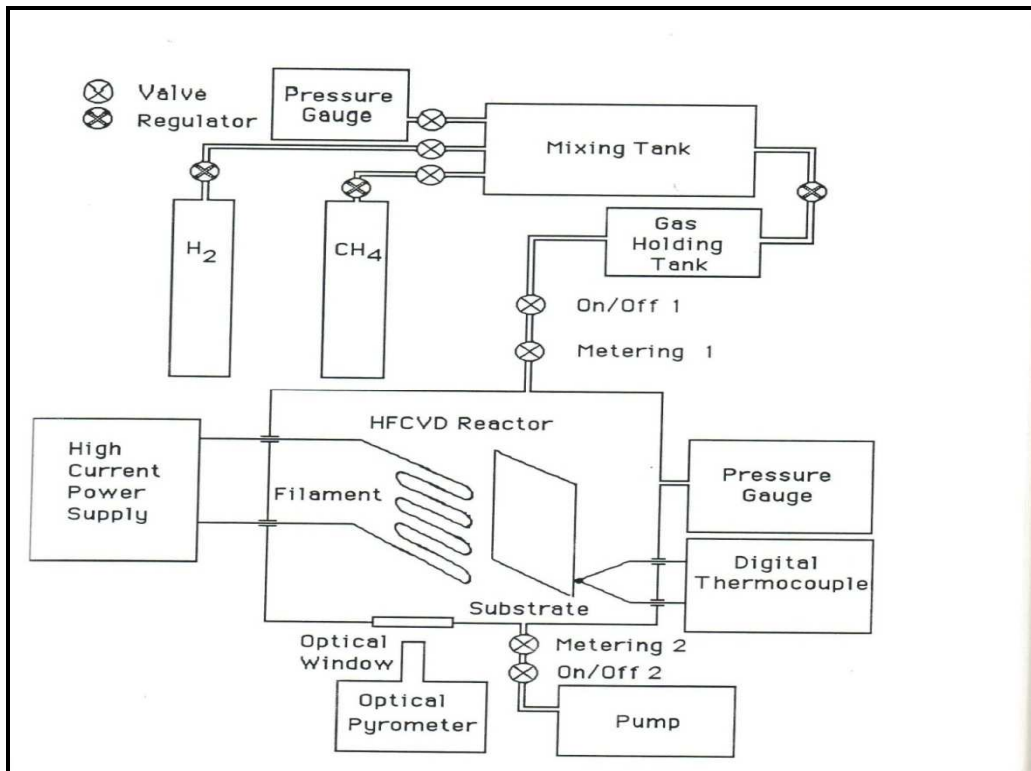


Figure 2.7 Block Diagram of CVD Furnace [6, 7, and 38]

During growth, the diamond surface is nearly fully saturated with hydrogen. The most likely fate for this surface site is for it to react with another nearby H atom, returning the surface to its previous stable situation. A large number of reactive H atoms close to the surface can quickly bond to any excess dangling bonds on the surface hence preventing surface graphitization. Atomic H is known to etch graphitic sp^2 carbon many times faster than diamond-like sp^3 carbon. Thus, the H atoms serve to remove back to the gas phase any graphitic clusters that may form on the surface, while leaving the diamond clusters behind. Moreover, hydrogen prevents the build-up of polymers which might ultimately deposit onto the growing surface and inhibit diamond growth.

CHAPTER 3

CHARACTERIZATION TECHNIQUES

3.1 Introduction

Atomic Force Microscopy, Raman Spectroscopy, Scanning Electron Microscopy and X Ray Diffraction were used to characterize the CVD diamond films. AFM shows the topography of the CVD grown diamond films. Raman spectroscopy confirms the presence of diamond /hexagonal diamond and other entities. SEM allows the observation of surface morphology with various growth conditions and X-ray Diffraction technique provides information on the crystal structure of the samples.

3.2 Atomic Force Microscopy

The AFM is one of the foremost tools for imaging, measuring, and manipulating matter at the nanoscale. The information is gathered by “feeling” the surface with a mechanical probe. Piezoelectric elements that facilitate tiny but accurate and precise movements on (electronic) command enable the very precise scanning. Binnig, Quate and Gerber invented the first atomic force microscope (also abbreviated as AFM) in 1986. The Atomic Force Microscope was developed to overcome a basic drawback with STM – that it can only image conducting or semiconducting surfaces. The AFM, however, has the advantage of imaging almost any type of surface, including polymers, ceramics, composites, glass, and biological samples.

An atomically sharp tip is scanned over a surface with feedback mechanisms that enables the piezo-electric scanners to maintain the tip at a constant force (to obtain height information), or height (to obtain force information) above the sample surface. Tips are typically made from Si_3N_4 or Si, and extended down from the end of a cantilever. When the tip is brought into

proximity of a sample surface, forces between the tip and the sample lead to a deflection of the cantilever according to Hooke's law. Depending on the situation, forces that are measured in AFM include mechanical contact force, Van der Waals forces, capillary forces, chemical bonding, electrostatic forces etc. Typically, the deflection is measured using a laser spot reflected from the top surface of the cantilever into an array of photodiodes.

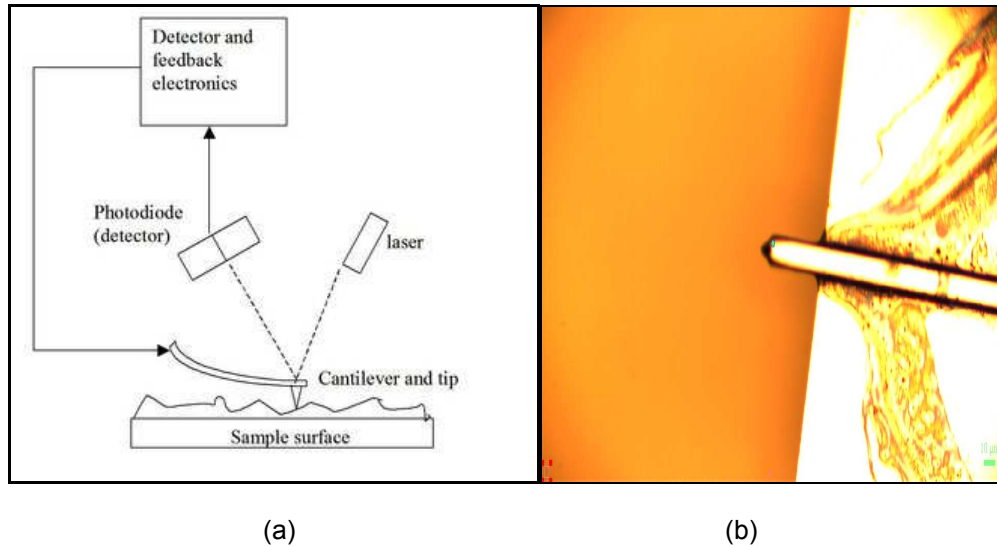


Figure 3.1 AFM (a) Working [29] and (b) AFM Tip

3.2.1 Imaging Modes

The primary modes of operation for an AFM are static mode and dynamic mode. In static mode, the cantilever is dragged across the surface of the sample and the contours of the surface are measured directly using the deflection of the cantilever. In the dynamic mode, the cantilever is externally oscillated at or close to its fundamental harmonic. These changes in oscillation with respect to the external reference oscillation provide information about the sample's characteristics.

3.2.2 Contact Mode

It is the most widely used mode of operation where the tip is scanned across the surface and there is deflection as it moves over the surface corrugation. The tip is constantly adjusted to

maintain a constant deflection, and therefore constant height above the surface. It is this adjustment that is displayed as data.

3.2.3 Non-Contact Mode

In this mode, the tip of the cantilever does not contact the sample surface. The cantilever is instead oscillated at a frequency slightly above its resonance frequency where the amplitude of oscillation is typically a few nanometers (<10 nm). The van der Waals forces, which are strongest from 1 nm to 10 nm above the surface acts to decrease the resonance frequency of the cantilever. This decrease in resonance frequency combined with the feedback loop system maintains a constant oscillation frequency by adjusting the average tip-to-sample distance. Measuring the tip-to-sample distance at each (x, y) data point allows the scanning software to generate a topographic image of the sample surface.

3.2.4 Tapping Mode

Tapping mode is applicable to general imaging in air, particularly for soft samples, as the resolution is similar to contact mode while the forces applied to the sample are lower and less damaging. In tapping mode, the cantilever oscillates close to its first bending mode resonance frequency, as in non-contact mode but the oscillation amplitude of the probe tip is much larger than for non-contact mode and tip makes contact with the sample for a short duration in each oscillation cycle. As the tip approaches the sample, the tip-sample interactions alter the amplitude, resonance frequency, and phase angle of the oscillating cantilever. During scanning, the amplitude at the operating frequency is maintained at a constant level, called the set-point amplitude, by adjusting the relative position of the tip with respect to the sample. In general, the amplitude of oscillation during scanning should be large enough such that the probe maintains enough energy for the tip to tap through and back out of the surface contamination layer. The only real disadvantages of tapping mode relative to contact mode are that the scan speeds are slightly slower and the AFM operation is a bit more complex, but these disadvantages tend to be outweighed by the advantages.

3.2.5 Instrumental Specifications

A Veeco Multimode SPM was utilized to carry on the topographic study of the samples. AC voltages applied to the scanner crystal X-Y axes produce a raster-type scan motion. The horizontal axis presented on the display monitor is referred to as the “fast axis” whereas orthogonal axis is known as the “slow axis”. Scanners with large scan ranges up to 125 microns on the XY axes and a Z range up to 5 microns, as well as high-resolution scanners with 0.4 microns on the XY axes and submicron Z range, are available. Utilizes advanced high-speed electronics along with A/D and D/A converters operating at 50MHz. A single controller regulates sample temperatures from -35 to 250°C.

Two types of tips were used in our experiments with the following specifications:

Table 3.1 Technical Specifications of the Tips used in AFM

Nanoworld Innovative Technologies	Veeco Instruments
Model : CONT – SPL POINT PROBE	Model : RTE – SPW
Coating: None [28]	Coating: Phosphorous (n) doped Si [29]
Thickness: 2 μm	Thickness : 3.75 μm
Frequency : 13kHz	Frequency : 300 kHz(max)

3.3 Scanning Electron Microscopy

Scanning Electron Microscope (SEM) is a type of electron microscope that images the sample surface by scanning it with a high energy beam of electrons in a Raster scan pattern (pattern of image detection and reconstruction in a television). Since the electrons have no color, it produces a black and white and 3 dimensional appearance of the image.

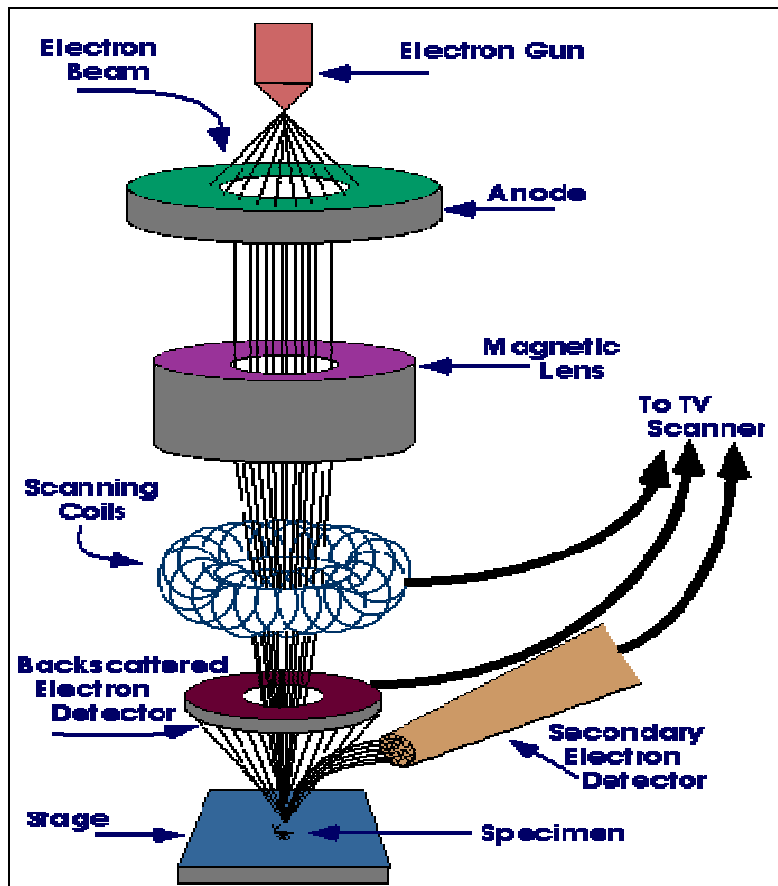


Figure 3.2 Components of SEM

3.3.1 Working

In SEM, electron beam is produced by the electron gun and focused on the sample. A large potential difference is produced between the cathode and anode, thereby causing the electrons to accelerate towards the anode. The collision of the electrons with the sample surface produces secondary electrons, whose intensity depends on the topography of the sample and is detected by the Secondary Electron Detector (SED) which is attached to a TV scanner to capture the image of the sample surface.

3.3.2 Resolution

Contrast and spatial resolution are the two main features that control image quality. Contrast is controlled by secondary electron emission density. Spatial resolution depends on the size of the electron spot which in turn depends on the magnetic electron-optical system producing the scanning beam. The resolution is also limited by the size of the interaction volume. The spot size and interaction volume are both very large compared to inter-atomic distances, so resolution of SEM is not high enough to image down to atomic scale as possible in TEM.

3.3.3 Wavelength Dispersive X-ray Spectroscopy (WDX)

Here X-rays are separated by diffraction and wavelengths of the dispersed X-rays from the sample are detected at different spectrometer positions. Hence results are plotted as counts Vs wavelength. In WDX, about 25-30% of the X-rays entering the detector are detected. WDX is often operated by positioning the crystal directly to the peak value so that the counting time is devoted to points of real interest. The limitations of WDX are small solid angle, long working distance etc.

3.3.4 Energy Dispersive X-ray Spectroscopy (EDX)

The working is quite similar to that of WDX but in comparison, data is collected in the form of dispersive X-ray energy and a diagram of counts Vs energy is plotted. EDX is cheaper compared to WDX.

3.3.5 Back Scattered Electron Imaging (BEI)

It consists of high energy electrons originating in electron beam that are reflected or back-scattered by elastic scattering from sample atoms. Back Scattered Electrons are sensitive to atomic weight since lighter elements cannot bounce back incident electrons much. Thus elements with higher atomic number produce brighter images. BSE is used to detect contrast between areas with different chemical composition.

3.3.6 Secondary Electron Imaging (SEI)

Unlike BSE the secondary electrons move slowly. Hence they can be attracted by a detector having a positive charge. This attractive force pulls the secondary electrons over a wide area of the sample. This ability to pull electrons from a wide area gives the image a three dimensional look. Hence SEI shows topography of a sample whereas BEI shows difference in composition.

A sample consisting of Cu and Al piece is placed inside SEM and analyzed as shown in Figure 3.3 (a, b, c).

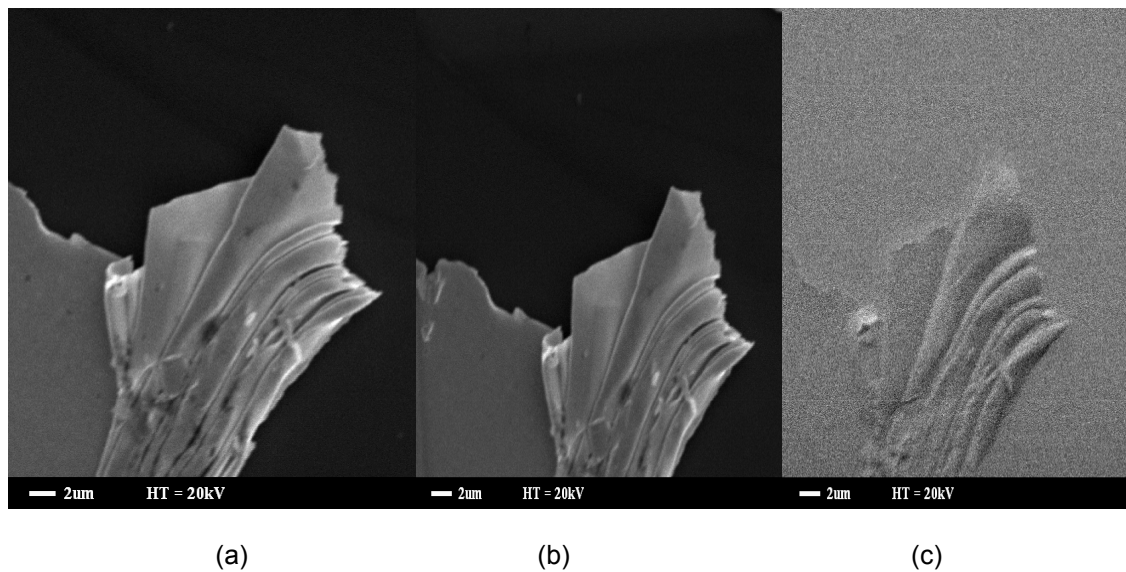


Figure 3.3 Cu and Al at Different Resolutions (a) SEI-1nA-15mm, (b) SEI-1nA-12mm and (c) TOPO-6nA-12mm

Figure 3.3.a. and Figure 3.3.b. are in COMPO mode. It is observed that the resolution and contrast of the surface is enhanced by increasing the working distance. Hence we can conclude that resolution is a function of working distance. Figure 3.3.c. is the image of the sample in TOPO mode. In TOPO mode the topography of the surface can be determined. Electrons coming from the top of a rough inclination produce bright intensity compared to a dark intensity of the lower inclinations. Hence in the image we observe various shades.

3.3.7 Instrumental Specifications

A ZEISS SUPRA 55 VP Scanning Electron Microscope connected to CCD Camera was used for analyzing the surface morphology of the diamond films. The microscope has a Schottky type field emission gun. The resolution of the images collected was 1nm @ 15kV. The system is attached to an Everhardt Thornley secondary electron detector. The GENESIS 4000 XMS system 60 Energy Dispersive Spectrometer performs the spectroscopic measurements with Xray mapping and digital imaging for SEM.

3.4 Raman Spectroscopy

Raman spectroscopy is a powerful tool to analyze gases, liquids and solids discovered by C.V. Raman in 1928 as Raman Effect which was further developed along with lasers and computer aided analysis into a sophisticated technique.

Raman scattering is an inelastic scattering of photons where the kinetic energy of the photons are not conserved. Raman Effect occurs when an incident beam of photons on a molecule/atom interacts with the electron cloud and excites the atom from its ground state to virtual state. The atom relaxes by emitting a photon and returns to a different rotational or vibrational state. The difference in energy between the states leads to a shift in the emitted photon's frequency away from the excitation wavelength. If the frequency of the emitted photon has lower frequency, the shift in frequency is designated as Stoke's shift. If the final vibrational state is less energetic than the initial state, then the emitted photon will be shifted to a higher frequency, and this is designated as an Anti-Stokes shift.

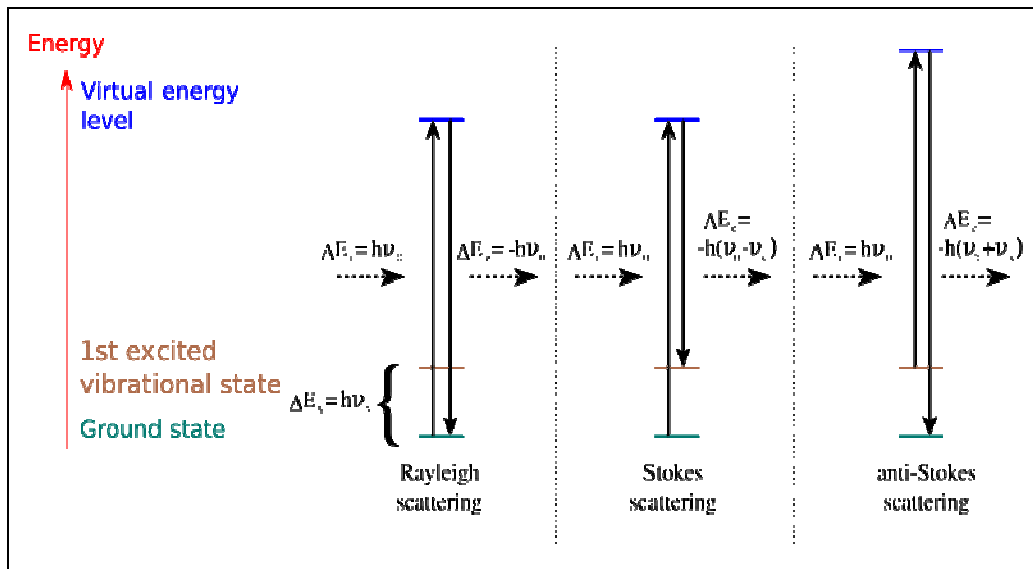


Figure 3.4 Energy Diagram of Raman Effect [30]

3.4.1 Physics of Raman Scattering

An incident electromagnetic wave induces a dipole moment during the light – material interaction where strength of the induced dipole moment, P , is given by

$$P = \alpha \vec{E} \quad (3.1)$$

Where α is the polarizability which is a material property and depends on the molecular structure and nature of the bonds and \vec{E} is the strength of the electric field of the electromagnetic wave. For the incident EM wave, the electric field may be expressed as

$$\vec{E} = E_0 \cos(2\pi\nu_0 t) \quad (3.2)$$

Where ν_0 is the frequency of the incident EM wave. Substituting equation (3.2) in equation (3.1),

$$P = \alpha E_0 \cos(2\pi\nu_0 t) \quad (3.3)$$

The physical displacement dQ of the atoms about their equilibrium position due to the particular vibrational mode may be expressed as

$$dQ = Q_0 \cos(2\pi\nu_{\text{vib}} t) \quad (3.4)$$

Where Q_0 is the maximum displacement about the equilibrium position and ν_{vib} are vibrational modes where the vibrational energy levels are quantized.

For a typical diatomic molecule the maximum displacement is about a small fraction of the bond length. For such small displacements, the polarizability may be approximated by a Taylor series expansion, namely,

$$\alpha = \alpha_0 + \frac{\partial \alpha}{\partial Q} dQ \quad (3.5)$$

Where α_0 is the polarizability of the molecular mode at equilibrium. Substituting equation (3.4) in the equation we get

$$\alpha = \alpha_0 + \frac{\partial \alpha}{\partial Q} Q_0 \cos(2\pi\nu_{\text{vib}} t) \quad (3.6)$$

Finally substituting equation (3.6) in equation (3.3), we get

$$P = \alpha_0 E_0 \cos(2\pi\nu_0 t) + \frac{\partial \alpha}{\partial Q} Q_0 E_0 \cos(2\pi\nu_0 t) \cos(2\pi\nu_{\text{vib}} t) \quad (3.7)$$

Using trigonometric identity we get

$$P = \alpha_0 E_0 \cos(2\pi\nu_0 t) + \left(\frac{\partial \alpha Q_0 E_0}{\partial Q} \right) [\cos[2\pi(\nu_0 - \nu_{\text{vib}}) t] + \cos\{2\pi(\nu_0 + \nu_{\text{vib}}) t\}] \quad (3.8)$$

Examination of the above equation reveals that induced dipole moments are created at three distinct frequencies which results in scattered radiation at these same three frequencies. The first scattered frequency corresponds to the incident frequency, hence is elastic scattering (Rayleigh), while the latter two frequencies are shifted to lower or higher frequencies and are therefore inelastic processes. The scattered light in these latter two cases is referred to as Raman scattering, with the down-shifted frequency (longer wavelength) referred to as Stokes scattering, and the up-shifted frequency (shorter wavelength) referred to as anti-Stokes scattering.

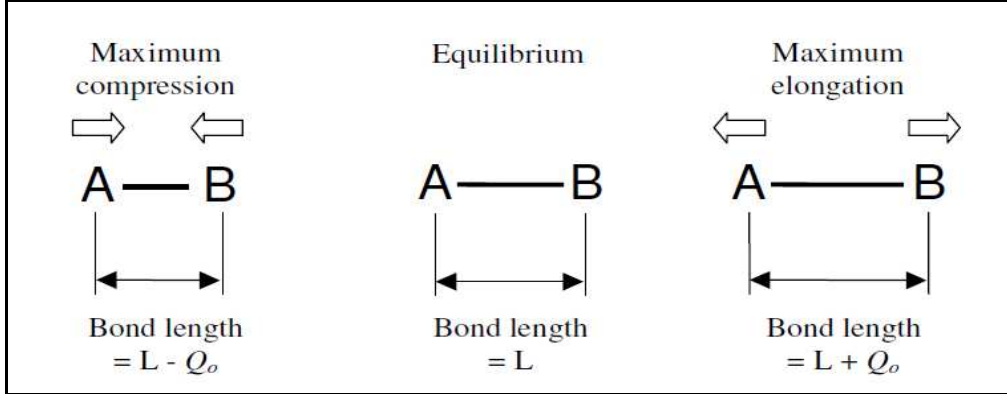


Figure 3.5 Vibrational Displacement of A-B about the Equilibrium Position [31]

3.4.2 Mathematical Model of Raman Scattering

From Maxwell-Boltzmann statistics, the number of particles corresponding to a given energy E_i in statistical equilibrium at temperature T is given by,

$$N_i = A \exp\left(-\frac{E_i}{kT}\right) \quad (3.9)$$

Where k is Boltzmann constant, A is coefficient determined by normalization.

The exponential is a decreasing function implying that the larger the $\frac{E_i}{kT}$ ratio, smaller the occupation number N_i . Considering two energy levels E_1 and E_2 the population ratios are given as,

$$\frac{N_{E_2}}{N_{E_1}} = \exp\left(-\frac{E_2 - E_1}{kT}\right) \quad (3.10)$$

$$\text{Where } E_2 > E_1 \quad (3.11)$$

$$\text{And } \Delta E = E_2 - E_1 = \frac{h\nu}{2\pi} \quad (3.12)$$

Thus population of lower energy state is greater than that of higher energy state leading to higher intensity Raman peaks in Stoke's case in comparison to Anti-Stoke's case.

3.4.3 Phonon Interaction

An incident photon creates an electron-hole pair in the material causing polarization in the solid allowing interactions with phonons. The electron/hole further emits a phonon (or absorbs a

phonon) after which a secondary photon is created by recombination of electron-hole pair. The Feynman diagrams of these processes are shown in Figure 3.6

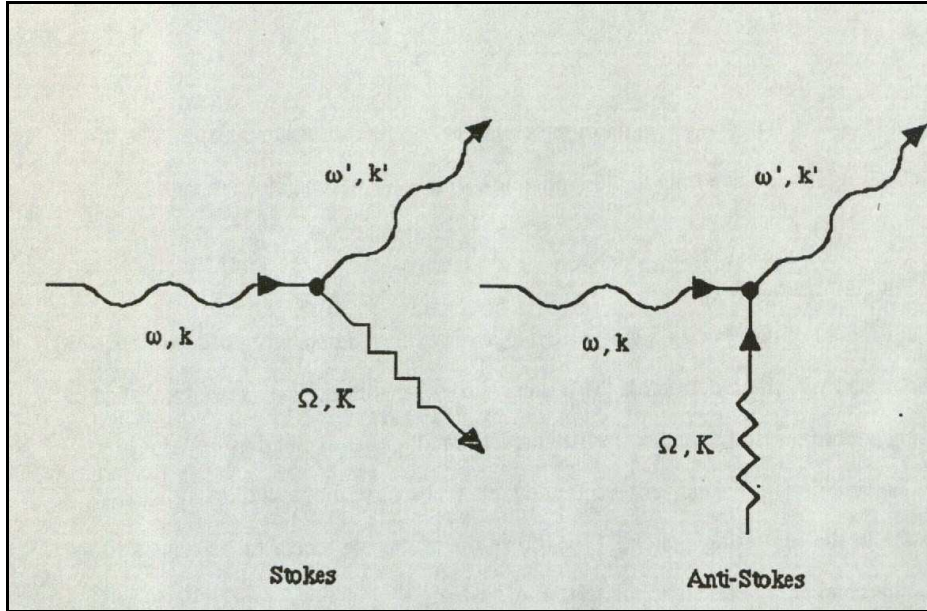


Figure 3.6 Feynman Diagrams of Phonon Interaction [32]

Due to conservation of energy, the first order selection rules for these transitions are given by

$$\omega = \omega' \pm \Omega \quad k = k' \pm K$$

Where ω and ω' are the frequencies of incident and scattered photon and Ω is the frequency of the phonon. The wave vectors k and k' are from incident and scattered photons and K is the wave vector for phonon. Stokes process is the creation of a phonon whereas the annihilation of a phonon corresponds to anti- Stokes process.

A phonon wave vector is related to the vibrational frequencies through the dispersion relation. The dispersion curve shows that vibrational excitations in a material exist within the Brillouin zone according to

$$0 \leq k \leq \frac{\pi}{a}$$

Where d is the crystal lattice constant and $k = \frac{2\pi}{\lambda}$. It is observed that wave vector of phonons is ~ 1000 times greater [33] than that of photons. Hence Raman scattering is sensitive only to those phonons with wave vector close to zero.

3.5 X- Ray Diffraction

Since the discovery of X-Rays by Wilhelm Conrad Rontgen, it is now a well known fact that X-rays are electromagnetic radiation of very small wavelengths ranging from 0.01 to 10nm and frequencies ranging from 30 petaHz to 30 exaHz. On the basis of energy or penetrating power X-rays can be classified as soft x-rays and hard x-rays. The typically used x-rays for material characterization are hard x-rays with energy from 12 to 120 keV. X-ray generation involves two mechanisms – Bremsstrahlung and Characteristic X-rays. Bremsstrahlung refers to ‘braking’ the radiation produced by acceleration of charged particles such as electron when deflected by another charged particle like the nucleus. Accelerated charges gives off electromagnetic radiation and when the energy of the bombarding electrons are high enough, the radiation falls in the x-ray region of the electromagnetic spectrum which is characterized by continuous distribution of radiation which intensifies and shifts towards higher frequencies when the energy of the bombarding electrons is increased. When electrons have sufficient energy to knock off inner shell electrons of a target material, characteristic x-rays are produced. These spectra consist of several components, the most common being K_{α} and K_{β} .

3.5.1 Diffraction and Bragg’s Law

Diffraction is defined as the apparent bending of waves around small obstacles and the spreading out of waves past small openings. Diffraction generally occurs when the propagating waves have the wavelength on the order of the size of the diffracting object. The main factor causing diffraction is the phase difference between the two waves.

Let us consider two parallel planes of atoms having the same Miller Indices and separated by inter planar spacing ‘ d ’. A parallel, coherent and monochromatic X-Ray beam of wavelength λ is

incident on these two planes at angle θ . Constructive interference of diffracted rays occur if path difference ABC is equal to a whole number multiple of wavelengths.

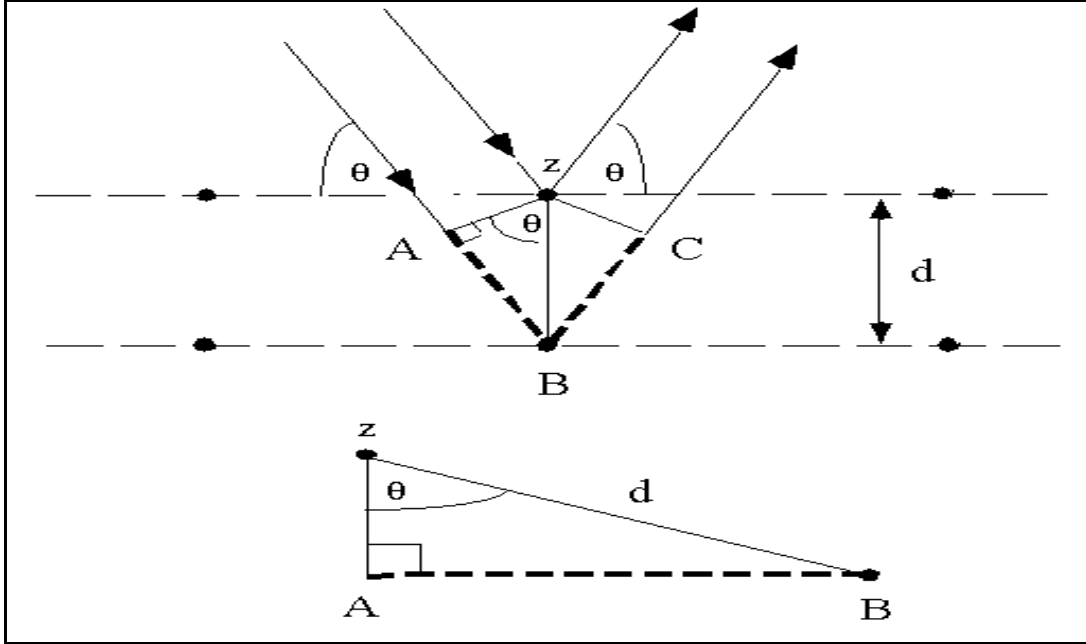


Figure 3.7 Diffraction off Crystal Planes

From the figure,

$$AB = d \sin \theta \quad (3.13)$$

$$AB + BC = 2d \sin \theta \quad (3.14)$$

$$n\lambda = AB + BC \quad (3.15)$$

$$n\lambda = 2d \sin \theta \quad (3.16)$$

The above equation is known as Bragg's Law.

The magnitude of the distance of separation between two adjacent parallel planes of atoms, i.e., the interplanar spacing d_{hkl} is a function of Miller indices (h, k, l) and lattice parameter (a). For example, for a crystal structure of cubic symmetry,

$$d_{hkl} = \frac{a}{\sqrt{h^2 + k^2 + l^2}} \quad \text{Where } a = \text{lattice parameter.}$$

3.5.2 Functions

XRD is a powerful and non-destructive technique to identify fine grained materials that are difficult to determine optically. Residual stress is the stress that remains in the material after the external force that caused the stress is removed. Stress analysis is based on measuring angular lattice strain distributions. That is, we choose a reflection at high 2θ and measure the change in d-spacing with different orientations of the sample. Using Hooke's law stress can be calculated. The texture of a sample is represented by pole figure. XRD is a very useful tool to study the texture.

CHAPTER 4

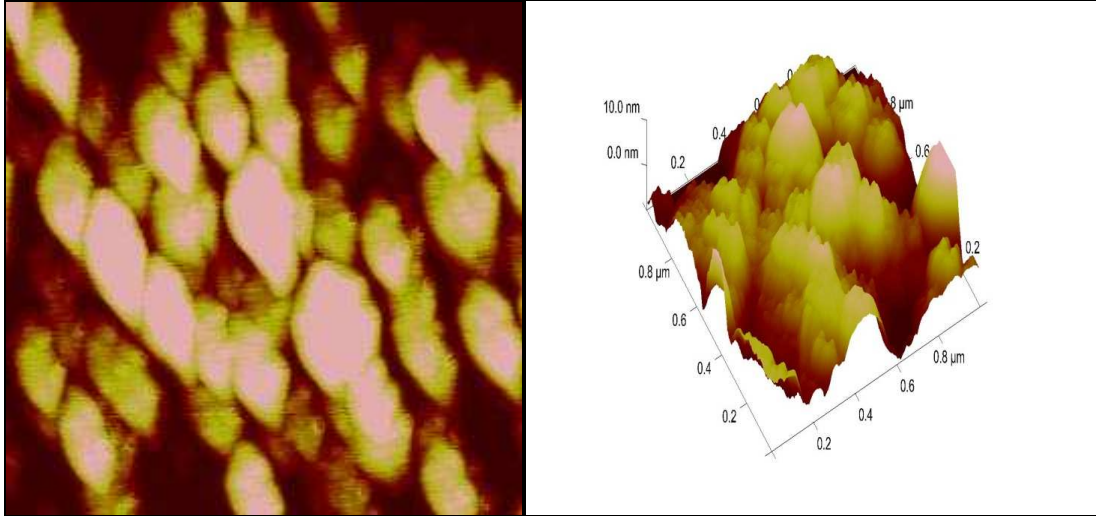
RESULTS AND DISCUSSION

4.1 Atomic Force Microscopy Results

AFM provides direct height measurements and unobstructed view of surface features. The microscopy was performed on the four samples namely SH76#1, SH76#2, SH76#3 and SH77#4 each having growth periods of 15, 30, 43 and 105 minutes respectively. For each one of the 15, 30 and 43 minutes samples, the AFM scan covers $1\text{-}\mu\text{m}^2$ surface area of the sample. For the 105 min sample, because of much larger diameter of the particles the AFM scan covers $3\mu\text{m} \times 3\mu\text{m}$ area of the sample.

4.1.1 AFM scan of SH76#1 (15 minutes)

Figure 4.1 shows the AFM image of the 15 minute sample with a scan range of $1\ \mu\text{m}$. The AFM image of the 15 minute sample shows particles of average size $\sim 50\ \text{nm}$. A rough surface is observed with average height of particles around $10\ \text{nm}$. The particles are smaller and densely packed as observed in the micrograph. The particle distribution is not very uniform. Grain boundaries are visible.



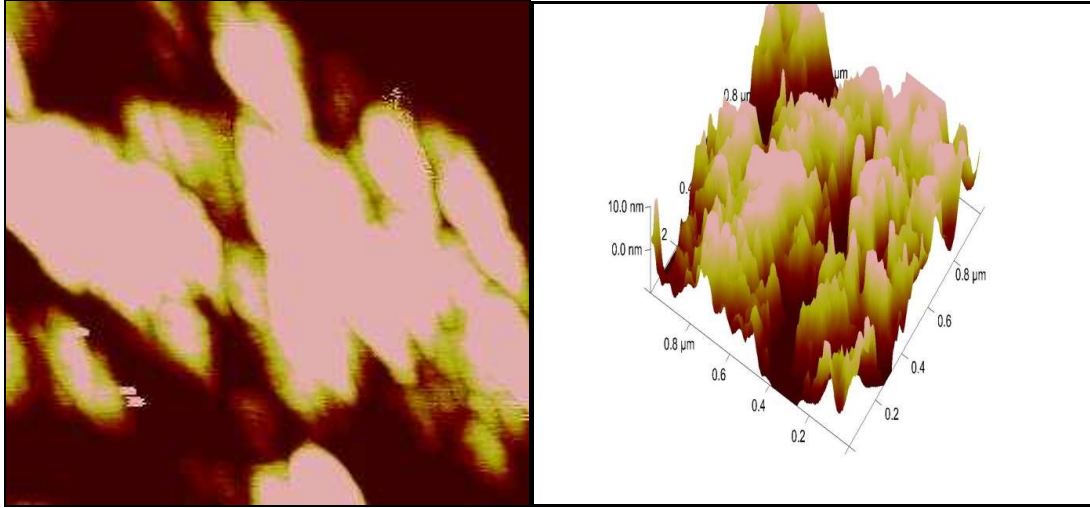
(a)

(b)

Figure 4.1 AFM Scan of 15 minutes sample (a) Top View and (b) Side View

4.1.2 AFM scan of SH76#2 (30 minutes)

The 30 minute sample shows particles with smoother surface and bigger size as observed in the micrograph. The particle distribution is more uniform as compared to the 15 minute sample. The micrograph in Figure 4.2 shows sharp grain features with some particles agglomerated. The average particle height is ~ 10 nm. However, some particles show a height of ~ 30 nm as observed in the side view in Figure 4.2. Most of the particles are in the size range of 50-60 nm.



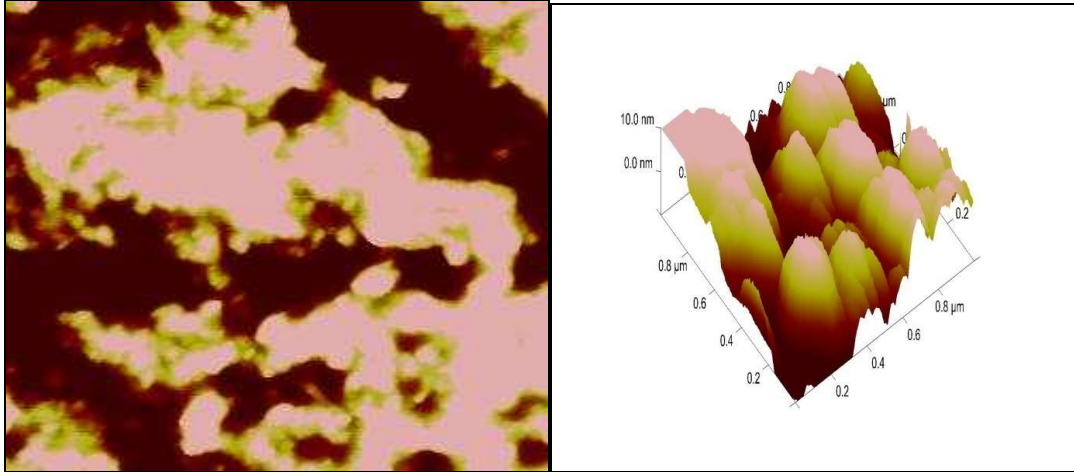
(a)

(b)

Figure 4.2 AFM Scan of 30 minutes sample (a) Top View and (b) Side View

4.1.3 AFM scan of SH76#3 (43 minutes)

The top view of SH76#3 (Figure 4.3.a) shows smooth boundaries with grains almost indistinguishable from each other. The roughness of the surface is observed to have reduced a lot. The particles are observed to agglomerate together. Deep dark patches are also observed which shows the area without diamond deposition. The particles are observed to grow more uniformly with an average height of 10 nm and sizes in the range of 60-70 nm.



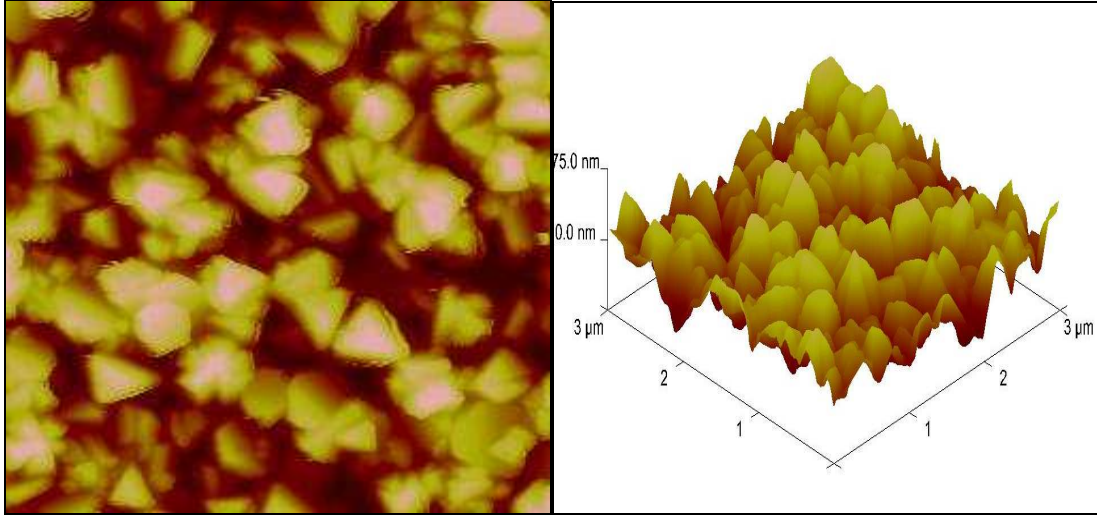
(a)

(b)

Figure 4.3 AFM Scan of 43 minutes sample (a) Top View and (b) Side View

4.1.4 AFM scan of SH77#4 (105 minutes)

AFM also provides a rough estimation of the particle sizes with growth period. It is observed that the particle sizes increase with growth period. In 105 min samples, the particles are clearly visible with a more uniform growth and distribution. The maximum height observed is of ~ 175 nm with particle sizes of ~ 200 nm. Comparing the micrographs in all samples, diamond deposited at longer growth period exhibits smooth grain features and less grain boundaries.



(a)

(b)

Figure 4.4 AFM Scan of 10.5 minutes sample (a) Top View and (b) Side View

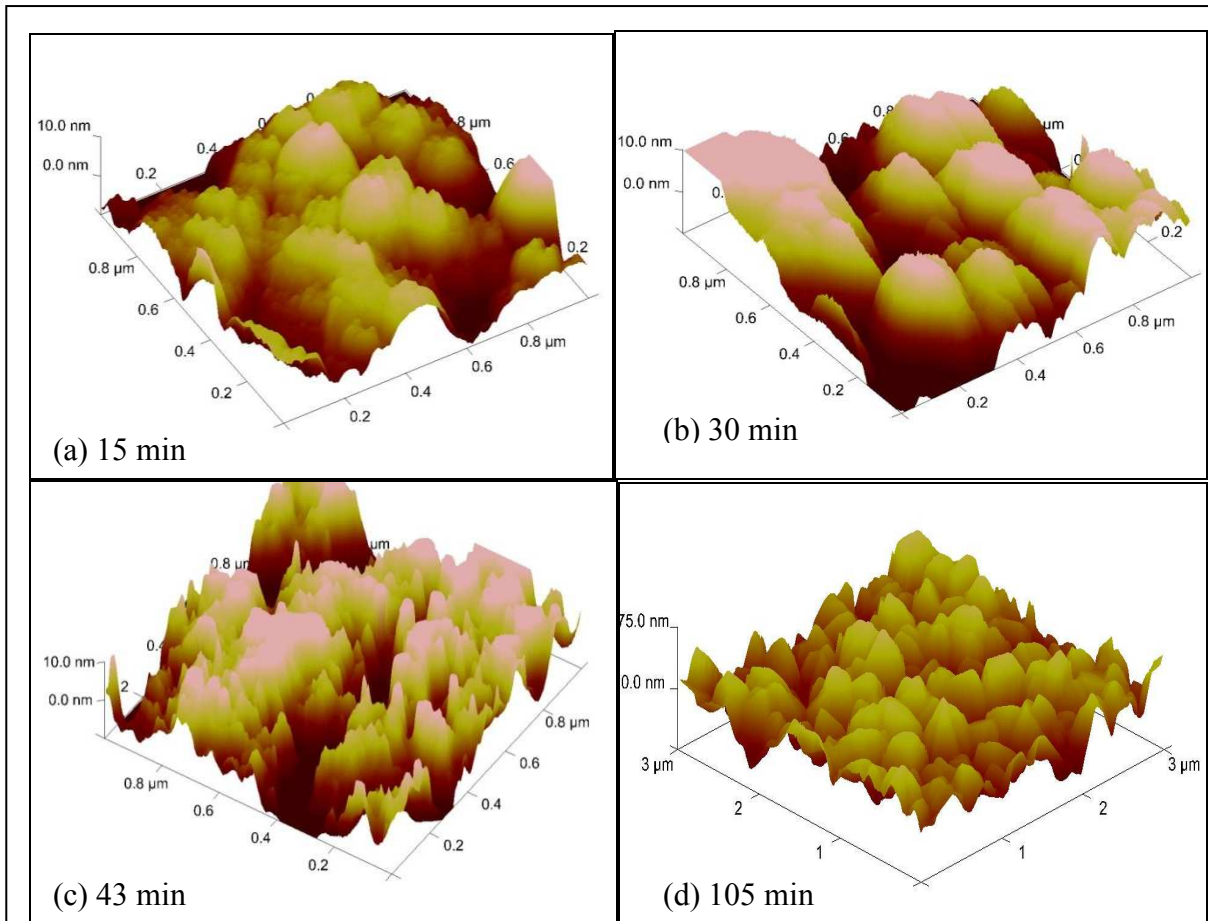


Figure 4.5 Relative Comparison between the AFM Images of Samples with Growth Period of (a) 15 (b) 30 (c) 43 and (d) 105 min respectively [35]

4.2 Scanning Electron Microscopy

Scanning electron microscopy permits quantitative observations of changing surface of the diamond films showing a change in surface morphology for diamond films grown at different time periods.

4.2.1 SEM image of SH76#1 (15 minutes)

The SEM images of 15 minute sample as shown in Figure 4.6 reveals a very non- uniform distribution of particles on the surface with average particle size of ~ 50 nm. The scratch marks are clearly visible which are the marks created by rubbing the surface with bulk diamond to create nucleation sites. The lower right side of the image shows a lower concentration of

particles as compared to the left side. Figure 4.7 shows a higher magnification of the surface with two green lines running vertically across a particle, showing the particle size.



Figure 4.6 SEM Micrograph of SH76#1 (15 minutes) – Low Resolution

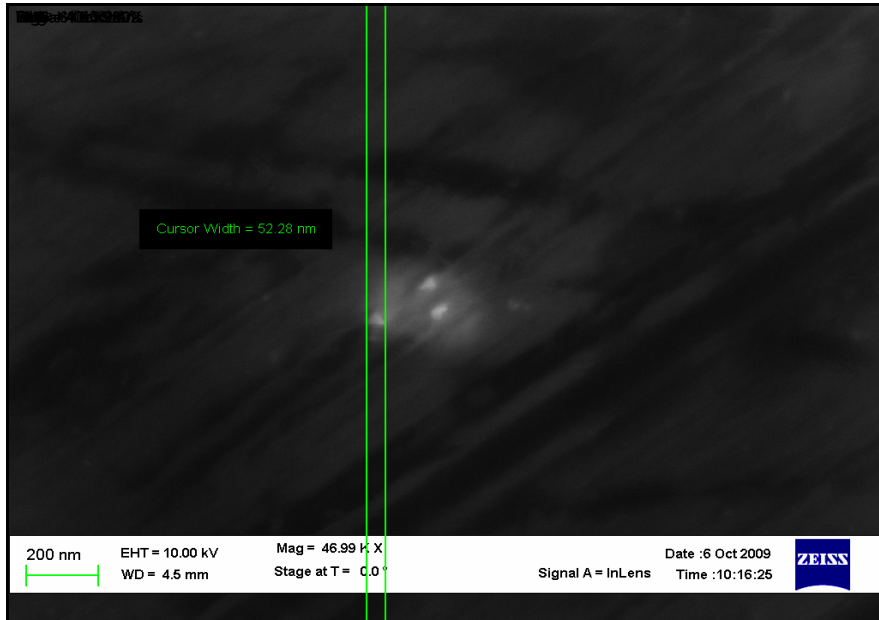


Figure 4.7 SEM Micrograph of SH76#1 (15 minutes) – High Resolution

4.2.2 SEM image of SH76#2 (30 minutes)

For the 30 minutes sample majority of the diamond particles are observed to be in the range of 40-50 nm. As the time increases, it is observed that the particles begin to grow more uniformly. The scratch marks are still visible on the surface. Some particles are observed to cluster together giving the appearance of a single big particle.

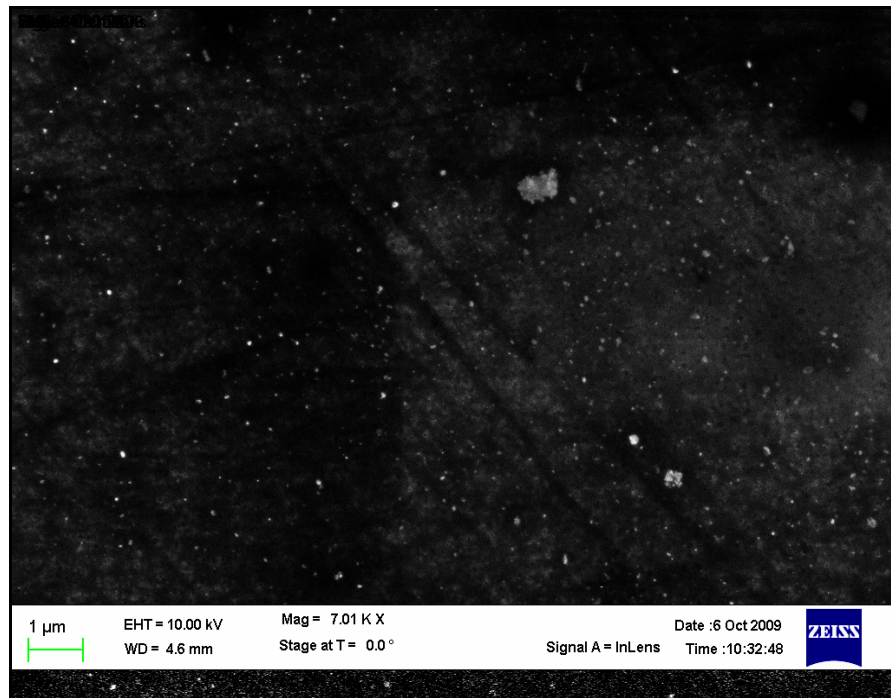


Figure 4.8 SEM Micrograph of SH76#2 (30 minutes) – Low Resolution

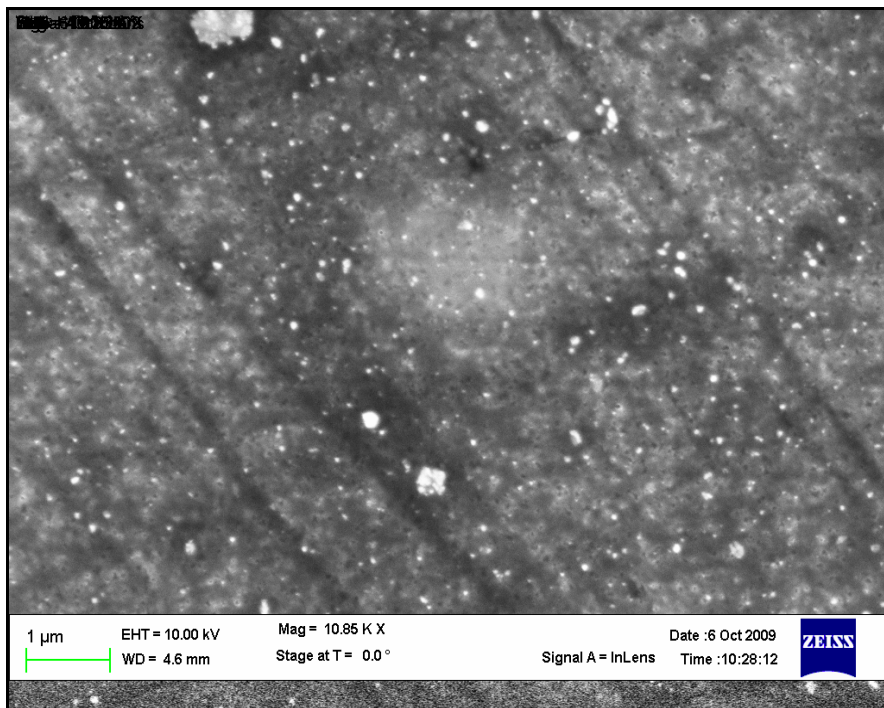


Figure 4.9 SEM Micrograph of SH76#2 (30 minutes) – High Resolution

4.2.3 SEM image of SH76#3 (43 minutes)

The morphology of the 43 minutes sample reveals a porous surface where diamond nanoparticles agglomerate along the fringes of the pores. The particles increase in size. It is assumed that the voids are the nucleation sites for crystal growth. Majority of the particles sizes are between 70-100 nm. There are indications of large voids of approximately 100 – 200 nm. A large particle of ~ 500 nm at the center of Figure 4.9 is a congregate form of diamond particles.

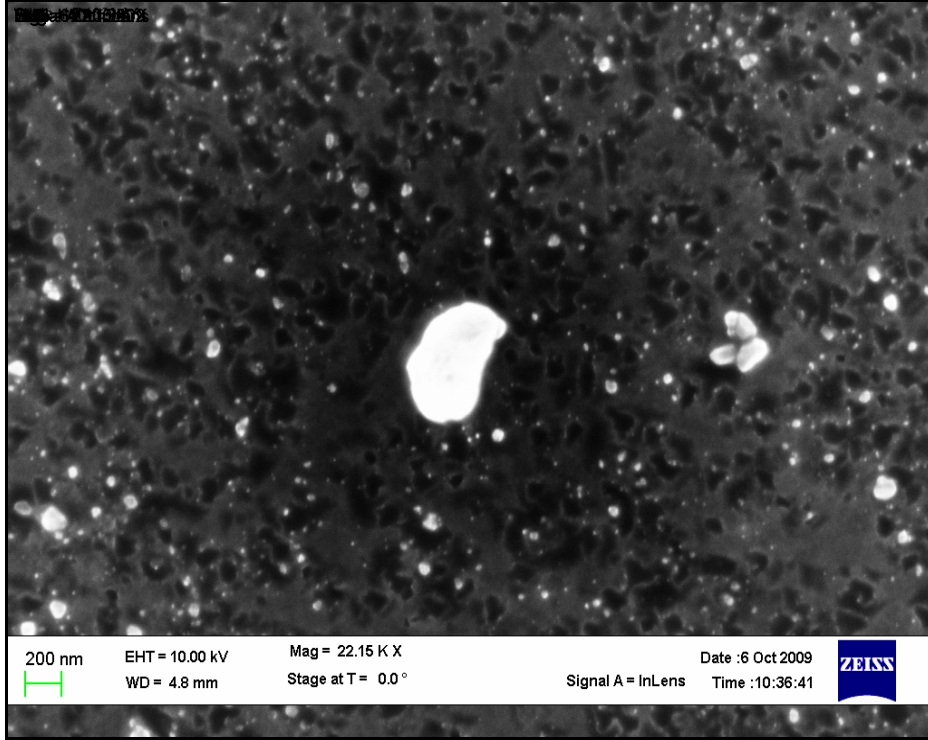


Figure 4.10 SEM Micrograph of SH76#3 (43 minutes) – Low Resolution

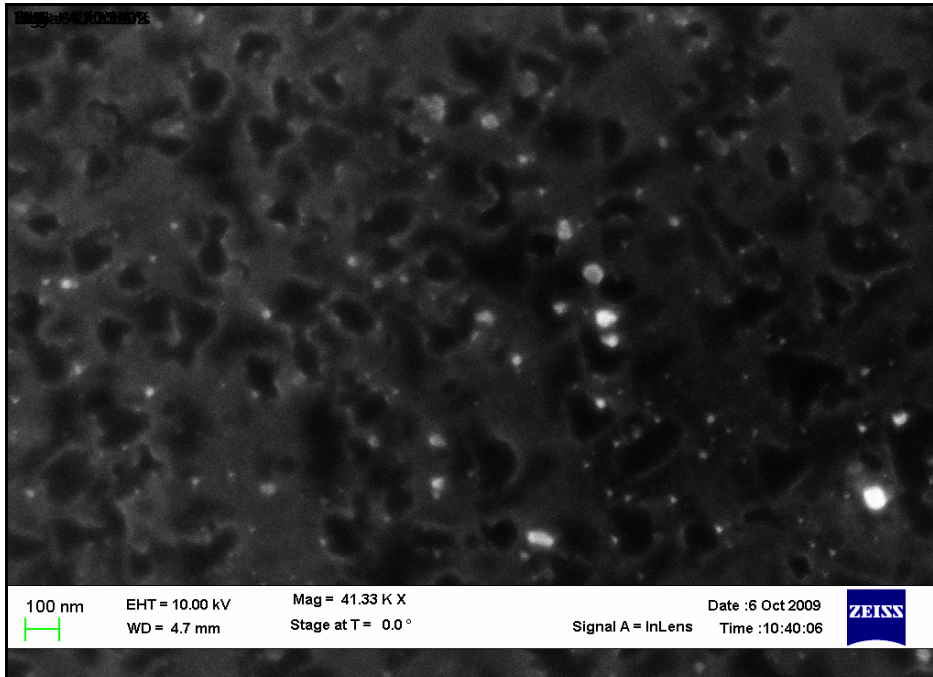


Figure 4.11 SEM Micrograph of SH76#3 (43 minutes) – High Resolution

4.2.4 SEM image of SH77#4 (105 minutes)

A high resolution SEM micrograph of the 105 minutes sample shows pop-corn like structures (Figure 4.12) of diamond nanoparticles clustered together with particle sizes between 100 – 200 nm. Particles are almost uniformly spread on the surface. A micrometer sized diamond particle with sharp edges is also seen in the micrograph (Figure 4.13). It is assumed to be a left over particle when the surface was scratched with diamond to form nucleation sites. A number of diamond particles aggregate on the surface of the diamond particle.

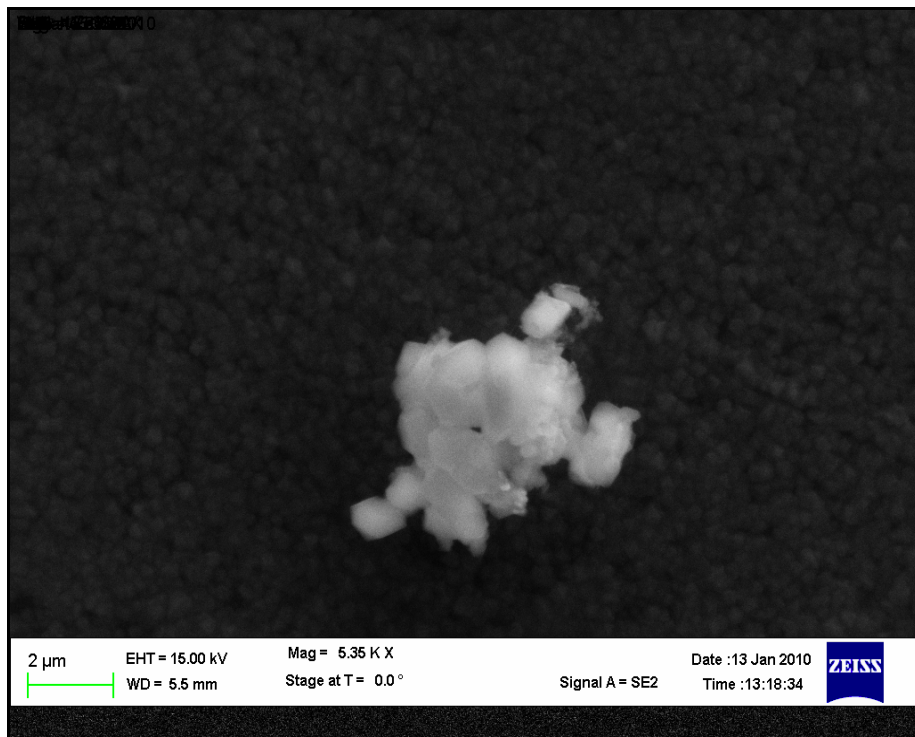


Figure 4.12 SEM Micrograph of SH77#4 (105 minutes) – High Resolution

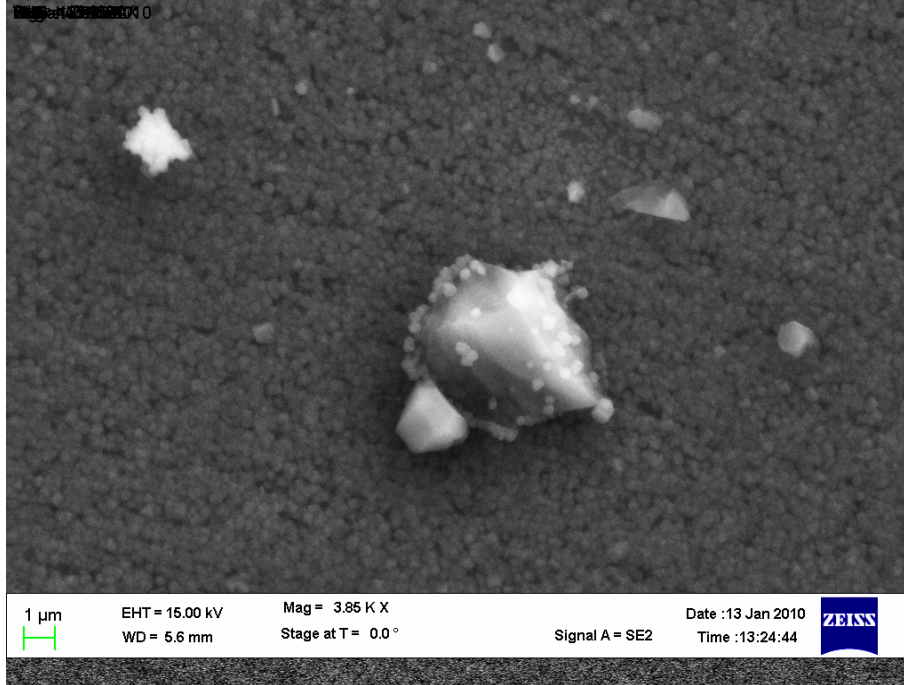


Figure 4.13 SEM Micrograph of SH77#4 (105 minutes) – Low Resolution

4.2.5 Particle size distribution

Further examination of these SEM images (Figure 4.6 – Figure 4.13) shows that particle size increases with growth period, starting from very small (~ 10 nm in 15 min sample) to large (~ 200 nm in the 105 min sample). This is in agreement with previous observation that the average size of the diamond particles increase linearly with growth period [36]. The micrographs resulting from these films were analyzed for particle size distribution. For better understanding of this process, the SEM micrographs were magnified and approximately 200 particles were examined for each sample. The results of the analysis are shown in Figure 4.14 and Table 4.1. Whereas in 15 minutes sample, the nanoparticles of 15 and 45 nm diameters dominate, the size distribution for 105 minutes sample approximates a Gaussian distribution centered around 200nm. The average diameters of the nanoparticles calculated from these histograms are included in Figure 4.15 (circles) which also shows results from previous experiments (straight lines). The line with greater slope represents mean grain size with growth rate of $0.0817\mu\text{m/h}$

with y intercept of 0.0047454 μm . The second line represents mean grain size with slope of 0.1662 $\mu\text{m}/\text{hr}$ with y intercept of 0.074596 μm [36].

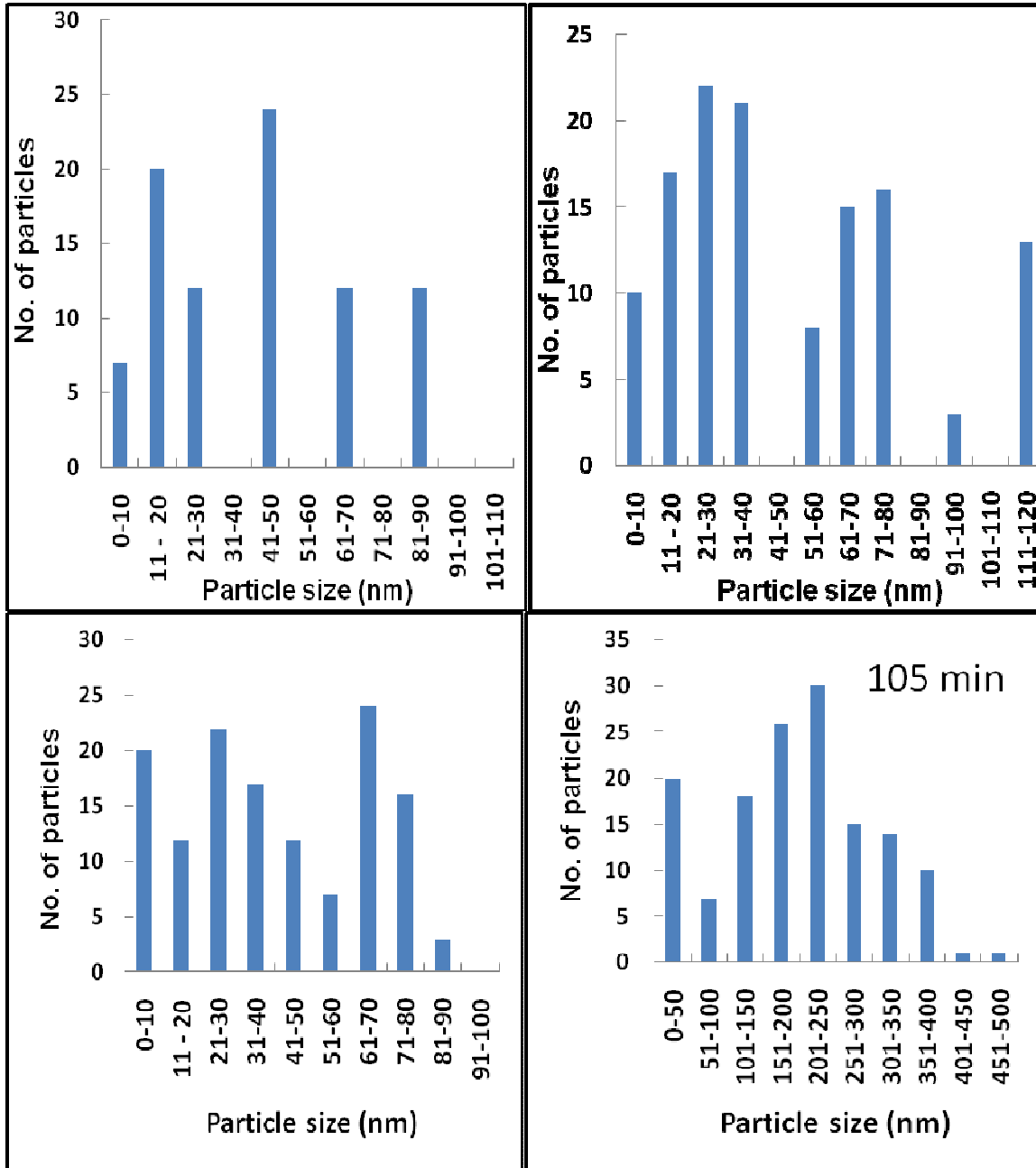


Figure 4.14 Particle Size Distributions of Diamond Nanoparticles (Clockwise from top left- 15, 30, 43 and 105 minutes) [35]

Table 4.1 Size Distribution of Diamond Nanoparticles

Sample	Growth Time (minutes)	Weighted Average Size (nm)
SH76#1	15	41.25 ± 8.5
SH76#2	30	70.34 ± 7.8
SH76#3	43	40.33 ± 8.04
SH77#4	105	196.4 ± 9.75

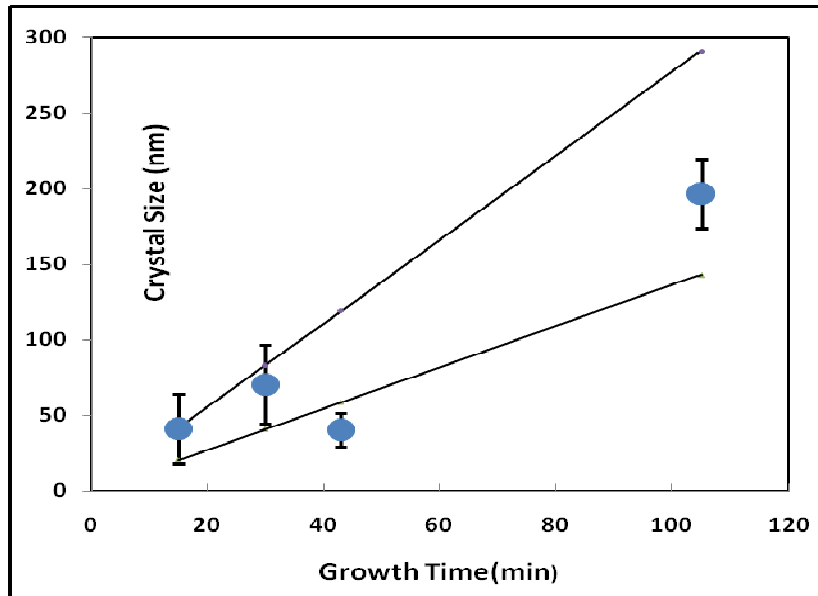
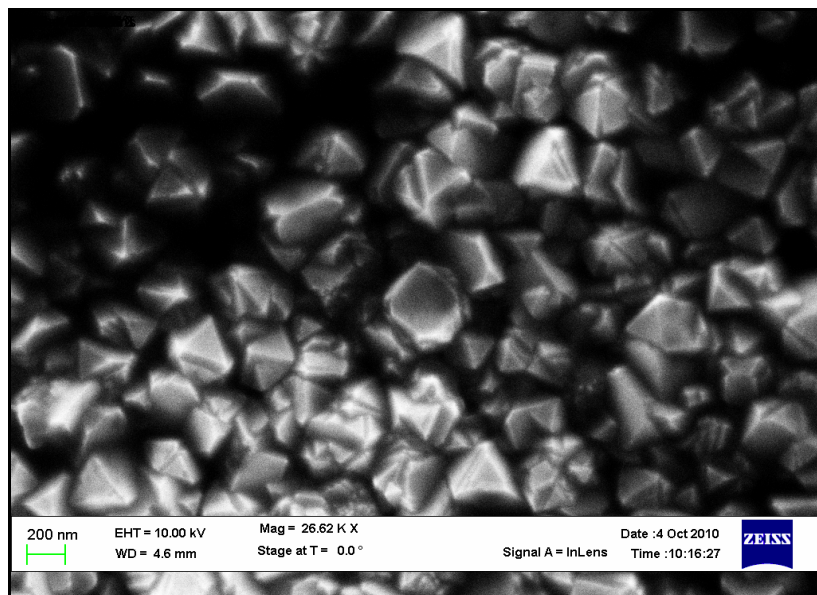


Figure 4.15 Crystal Size Vs Growth Time

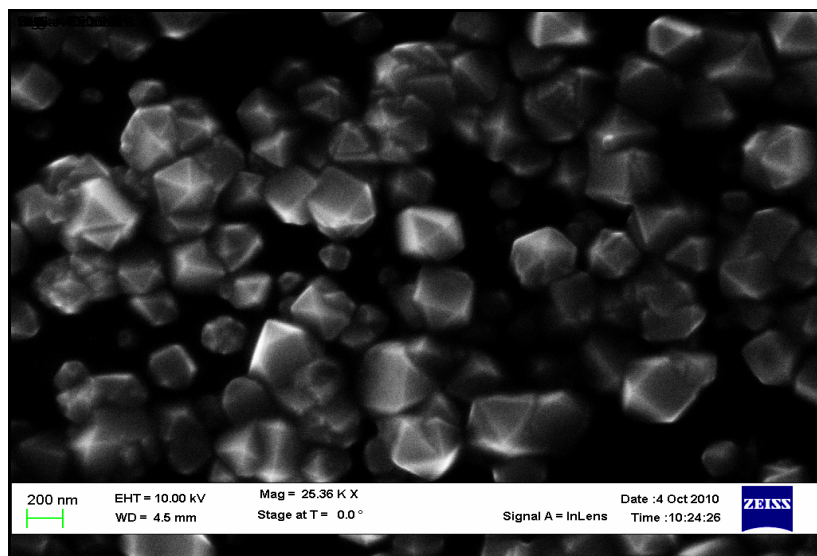
4.2.6 SEM Results of Hexagonal Nanodiamonds

Figure 4.16 – Figure 4.17 shows the SEM micrographs of sample SH77#4 (105 min). The crystallites display a multitude of triangular faces indicating (111) crystal face of a cubic structure. The Raman results of hexagonal diamonds are consistent with SEM micrographs. Twinning along (111) faces is also observed. Hexagonal particles smaller than 50 nm were not observed. However, their presence cannot be ruled out since the resolution is not good enough

to discern the shape information. The mechanism of formation of hexagonal nanoparticles can be explained by twinning which is extremely sensitive to local stresses.



(a)



(b)

Figure 4.16 SEM Micrograph of SH77#4 (a) and (b) High Resolution

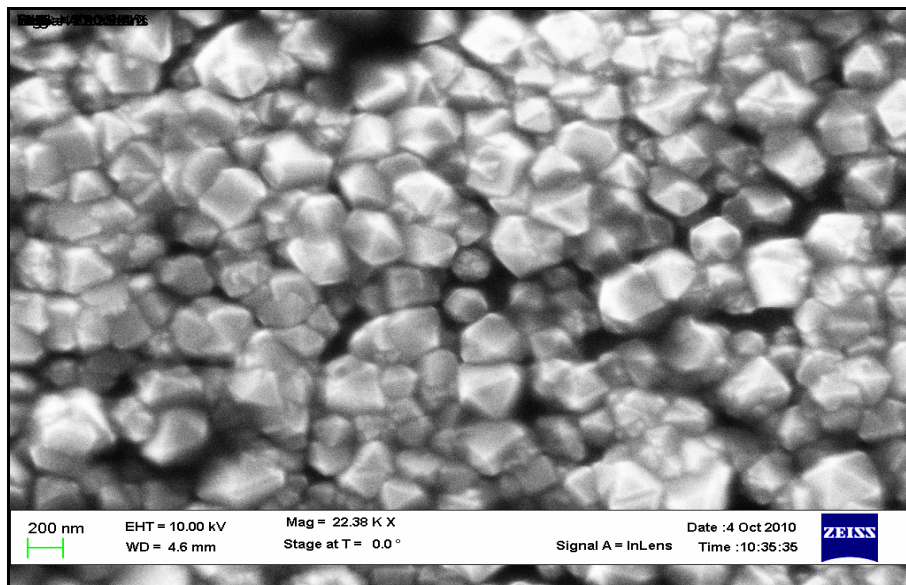
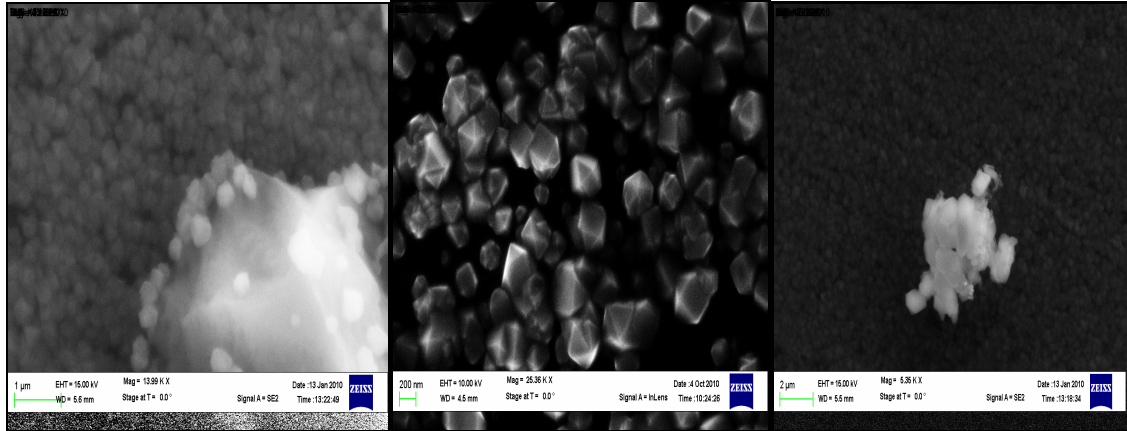


Figure 4.17 SEM Micrograph of SH77#4 - Low Resolution

4.2.7 Particle Size Distribution of Hexagonal Nanodiamonds

To understand the particle size distribution of hexagonal particles we examined around 200 particles. The micrographs as shown in Figure 4.18 were analyzed to generate the particle size distribution histogram. The histogram in figure shows the size distribution of both cubic and hexagonal nanoparticles. The size distribution can be represented by a Lorentzian function with average size around (190 ± 25) nm. The concentration of hexagonal nanoparticles were calculated to be around 10% of sizes ranging from 50 – 400 nm (grey shade) as shown by the histogram (red shades) in Figure 4.19



(a) (b) (c)

Figure 4.18 SEM Micrographs used for Particle Distribution (a), (b) and (c)

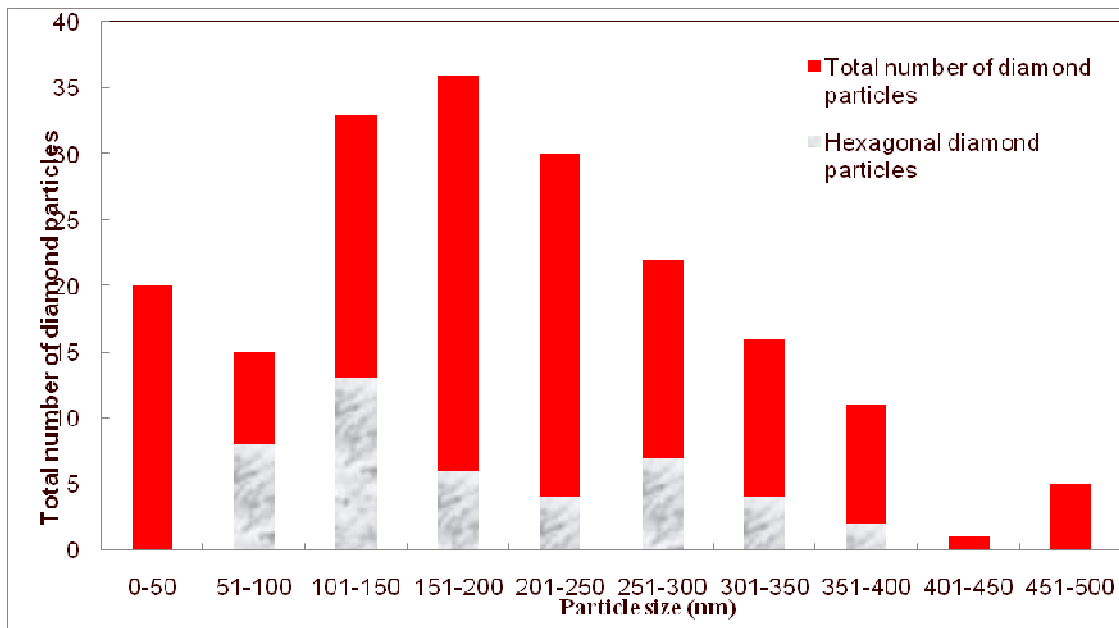


Figure 4.19 Particle Size Distributions of Hexagonal Nanodiamonds

4.3 Raman Spectroscopy Results

Raman spectroscopy was performed on all samples to detect the presence of diamond in the CVD grown thin films. The presence of carbon allotropes in the films are distinguished by their Raman active vibrational modes. Diamond has a characteristic sharp peak at 1332 cm^{-1} .

4.3.1 Natural Diamond

Natural diamond of white 0.75 carat type 1A was analyzed as a reference sample. Figure 4.20 shows the Raman spectrum of natural diamond with a very sharp peak of high intensity at 1332 cm^{-1} . The full width at half maximum was recorded to be 3.485 cm^{-1} . No fit has been made to the data. There is no evidence of graphite or other carbon allotropes in the sample. Information about the quality of the crystal can be obtained from analysis of diamond peak. Defect free diamond exhibits narrow and sharp peak at 1332 cm^{-1} and the peak broadens due to scattering off defects in the sample [37]

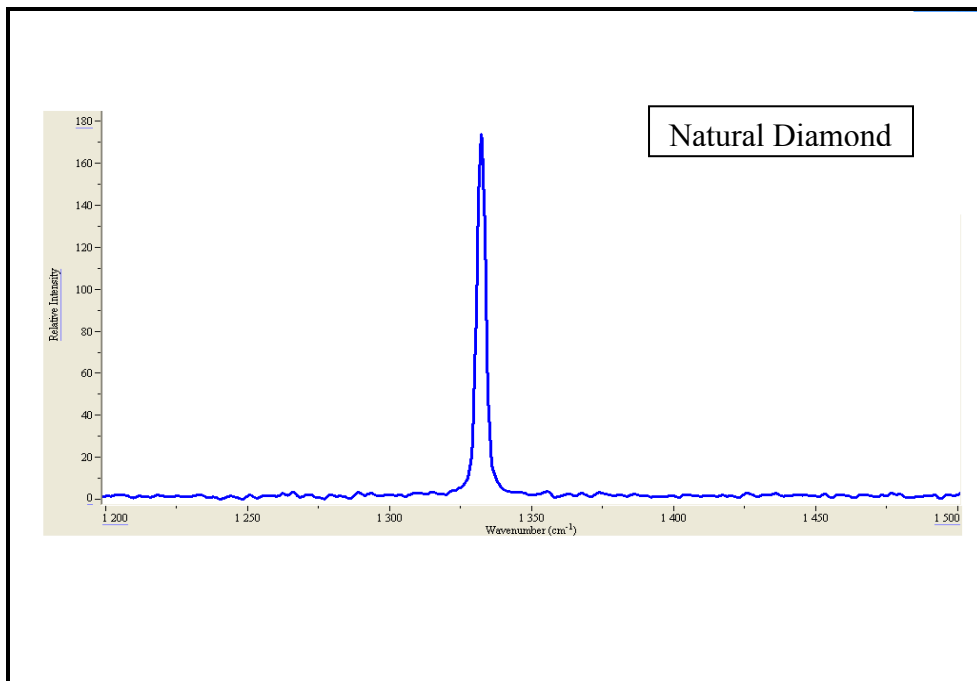


Figure 4.20 Raman Spectrum of Natural Diamond

4.3.2 Raman Results of Samples

Raman spectra of diamond films usually exhibit three features:(1) a sharp peak at $\sim 1332 \text{ cm}^{-1}$ which is the characteristic of crystalline diamond (FWHM $\sim 3.48 \text{ cm}^{-1}$ as measured for the sample which could be even sharper as measured before) representing the first – order zone center phonon mode of diamond structure, (2) a broad peak around 1500 which is the characteristic feature of diamond like carbon and (3) a broad peak around 1580 representing polycrystalline graphite or amorphous carbon [38,39]. The Raman spectra measured for our

samples show two bands within $1332 - 1338 \text{ cm}^{-1}$ as well as broader peaks centered within $1200 - 1260 \text{ cm}^{-1}$ and $1436 - 1600 \text{ cm}^{-1}$. The broadening of the 1332 cm^{-1} peak is attributed to the size of diamond crystalline domain [40,41]. We observe two bands centered within $1200-1260$ and $1436-1600 \text{ cm}^{-1}$. The broadening of the peaks is produced by a combination of several effects namely phonon confinement and scattering from defects. Internal stresses due to lattice mismatch between film and substrate can also cause broadening of peaks in the Raman spectrum. Previous experiments on several thin film diamond samples including SH76#1, SH76#2, SH76#3 and SH76#4 showed that the samples contain lattice vacancies and microvoids with relative concentration ranging from 10^{-5} to 0.1. Hence it can be stated that the lattice defects are high enough to contribute to both line broadening as well as shift from the 1332 cm^{-1} diamond line. This study further showed that the relative concentration of defects varies with the CVD growth parameters [36].

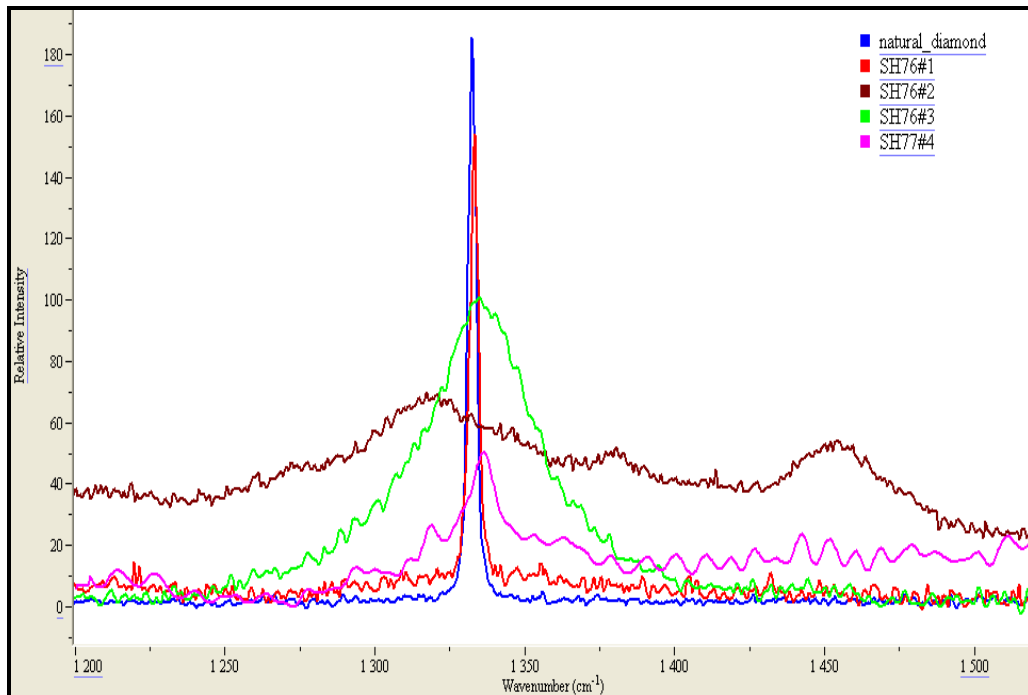


Figure 4.21 Raman Spectra of Samples

To get a better understanding of the Raman spectra and identify the presence and concentration of diamond in all the four samples, Raman spectra were smoothed and fitted with a Gaussian function. The 15 minute sample (A) shows a sharp peak confirming the presence of diamond along with a very small band centered at $\sim 1225 \text{ cm}^{-1}$, the origin of which is unknown. No presence of graphite or other carbon allotropes are observed. The 30 minute sample (B) shows a prominent diamond peak at 1332 cm^{-1} along with a broad band centered at $\sim 1330 \text{ cm}^{-1}$. In addition to the diamond peak, other bands centered at 1250 cm^{-1} , 1450 cm^{-1} and a graphite band $\sim 1600 \text{ cm}^{-1}$ are also observed. The 43 minute sample (C) shows a broad peak at $\sim 1330 \text{ cm}^{-1}$ along with a broad band which arises from defect scattering in the sample. The graphitic band at $\sim 1620 \text{ cm}^{-1}$ is also observed. The 105 minute sample (D) shows a small band at 1205 cm^{-1} which is assumed to be the characteristic Raman line for hexagonal diamond [42]. A sharp peak at around 1333 cm^{-1} confirms the presence of diamond along with two broad bands at $\sim 1450 \text{ cm}^{-1}$ and a graphitic band at $\sim 1550 \text{ cm}^{-1}$. It is observed that the concentration of graphite increases with growth period as confirmed by concentration calculations (discussed in the next section).

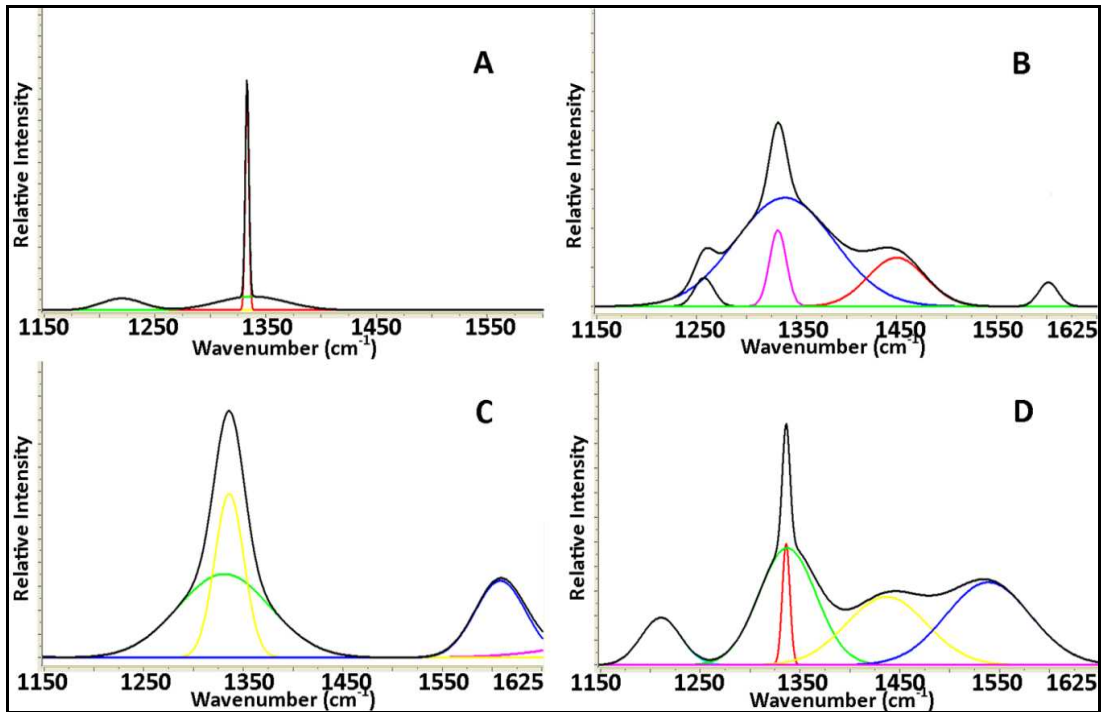


Figure 4.22 Raman Spectra of Samples (Noise Removed)

4.3.3 Concentration Calculations

By assuming that Raman scattering efficiency for non-diamond component is 50 times higher than diamond [36] we obtain diamond concentration results as shown in Figure 4.23. Calculated values show a decrease in relative diamond concentration from 99% in the 15 minutes sample to about 96% in the 105 minutes sample.

Table 4.2 Calculated Diamond Concentrations

Sample	Deposition time (mins)	Diamond conc (%)	Error (%)
SH76#1	15	99.437	± 5.97
SH76#2	30	99.37	± 4.6
SH76#3	43	99.32	± 2.22
SH77#4	105	96.513	± 4.54

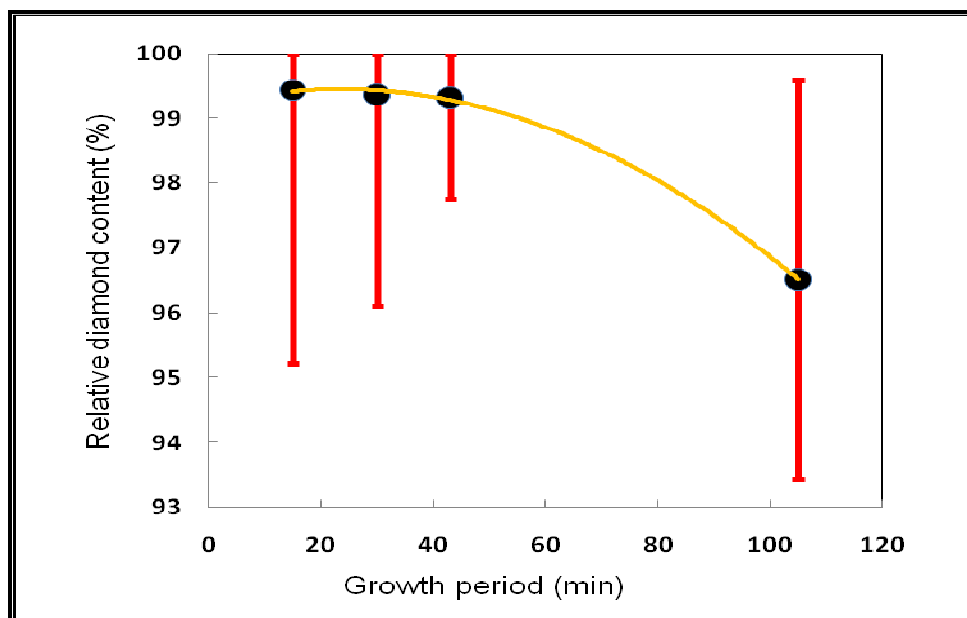


Figure 4.23 Relative Diamond Concentration Vs. Growth Time [35]

4.3.4 Phonon Confinement

The Raman spectra of the samples were observed to show an asymmetric broadening with particle size as shown in Figure 4.26. Defects or grain boundaries in a crystal can confine the phonons and the resulting changes in the Raman spectra can be used to estimate the dimensions of nanostructures. Phonon confinement model (PCM) [43] has been developed to correlate the observed changes in the crystallite. Within a nanocrystal a plane wave like phonon cannot propagate beyond the boundary, hence the wave function decays to a very small value at the crystal boundary. A confinement function accounts for the decay of the wave function and phonon contributions away from the center of the Brillouin Zone. A theoretical model was proposed by Richter et.al [43] to explain the observed shift to lower frequency and the broadening of the Raman line. The phonon-confinement model is based on the fact that in an infinite crystal, crystal momentum conservation limits Raman spectroscopy to observe phonons at the Brillouin zone center. However, a phonon can be confined in space by microcrystal

boundaries in a crystal with finite size. This leads to uncertainty in the phonon momentum which allows phonons with $q=0$ to contribute to the Raman signal. When the momentum uncertainty is convolved with the dispersion curve, the calculated Raman line shape becomes asymmetrically broadened and the maximum shifts to a lower frequency as the particle size decreases. The asymmetry arises because of the contribution of phonons away from the Brillouin-zone center to the Raman scattering process due to the relaxation of the $q=0$ selection rule in the case of a small particle.

4.3.5 Phonon Confinement Model

Assuming a Gaussian confinement function [9], the Raman Intensity is given as

$$I(\omega) = \int_0^1 \frac{\exp\left(-\frac{q^2 L^2}{4}\right)}{[\omega - \omega(q)]^2 + \left(\frac{\Gamma_0}{2}\right)^2} dq \quad (4.1)$$

Where q is the wave vector of a phonon in an infinite crystal, Γ_0 is the natural line-width of the zone center Raman line, L is the crystal size and $\omega(q)$ is the phonon dispersion relation.

$$\Omega(q) = A + B\cos(q\pi) \quad (4.2)$$

Where $A = 1241.25 \text{ cm}^{-1}$ and $B = 91.25 \text{ cm}^{-1}$ [43]

In this model, the line width Γ_0 is dependent on the crystal size L [44] according to,

$$\Gamma_0 = \alpha + \frac{\beta}{L} \quad (4.3)$$

Parameter α is the FWHM of the Raman spectrum measure for natural diamond (3.485 cm^{-1}) and parameter β is obtained (1200) from fits made to our Raman spectra.

In order to improve the agreement between the predictions of the model and experimental Raman spectra of ND, effects such as crystal size distribution, lattice defects, and the energy dispersion of the phonon modes were incorporated into the PCM. The particle sizes calculated are shown as triangles in Figure 4.24 where the PCM fitted to the SH76#3 is shown in the inset in Figure 4.25.

Table 4.3 Calculated Particle Size from PCM

Sample #	Growth Time (min)	Crystal Size (PCM)	FWHM Γ (cm^{-1})
SH76#1	15	20	63.485
SH76#2	30	24.8	51.8721
SH76#3	43	30.12	43.32
SH77#4	105	60	23.485

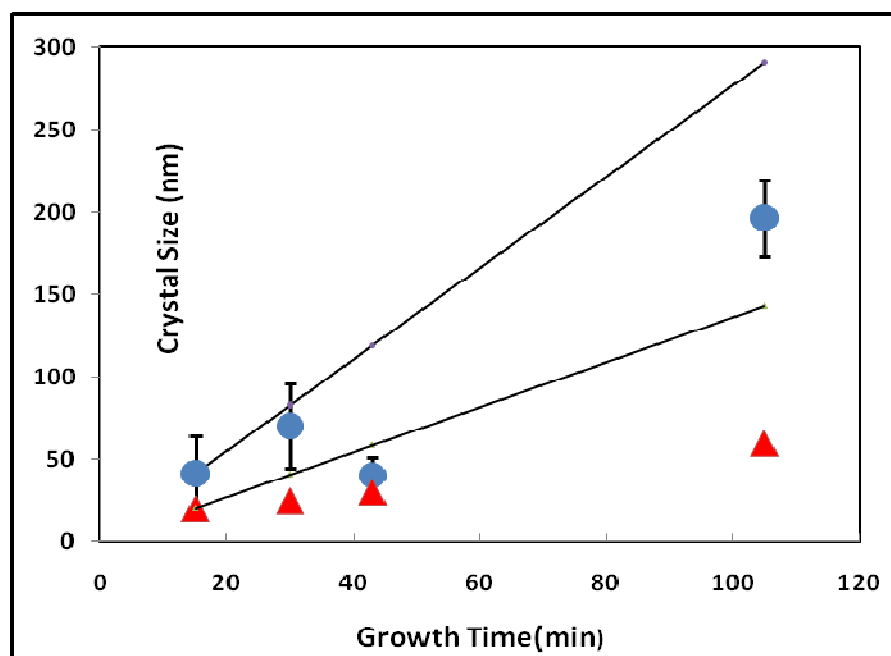


Figure 4.24 Crystal size Vs. Time [35]

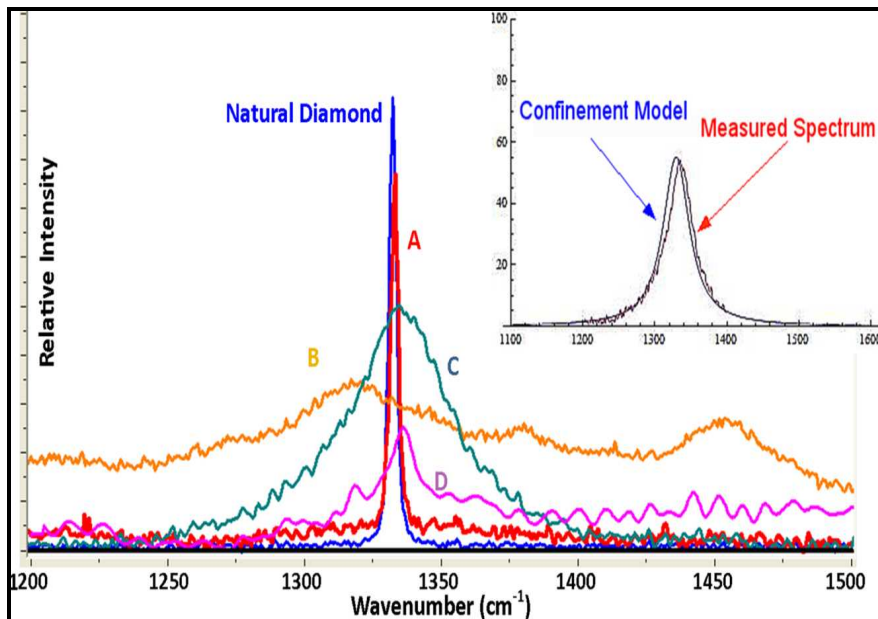


Figure 4.25 PCM Fitted to Data

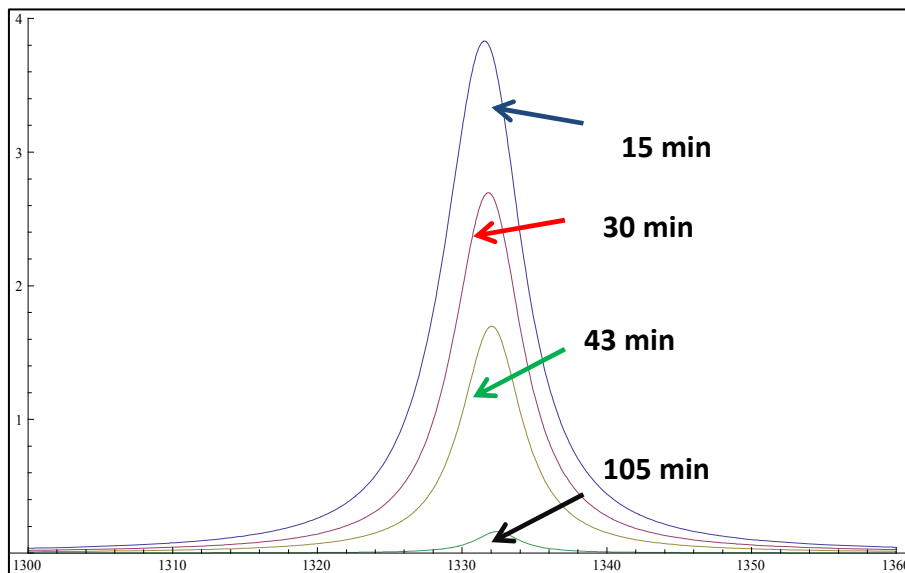


Figure 4.26 Asymmetric Peak Broadening (Theoretical Calculations)

4.3.6 Raman Spectroscopy Results for Hexagonal Nanodiamonds

Figure 4.27 shows Raman spectrum measured for SH77#4. The spectrum shows several bands centered at 1205 cm^{-1} , 1336 cm^{-1} , 1337 cm^{-1} , 1436 cm^{-1} and 1538 cm^{-1} . It is known that in samples containing micro crystallites smaller in size than the phonon decay lengths ($\ll 1\mu\text{m}$),

an increase in the phonon scattering off grain boundaries gives rise to lifetime-broadened peaks which are shifted from 1332 cm^{-1} [45,46]. By using first principles method based on density functional theory, Wu and Xu have calculated vibrational frequencies at the Γ point for both cubic and hexagonal diamond [47]. As far as the first-order zone-center mode of cubic diamond is concerned, there is a good agreement between calculated (1334cm^{-1}) and observed frequencies (1332cm^{-1}). The results of Zhu et al [42], who observed a strong line at 1199cm^{-1} in the Raman spectrum of hexagonal nanodiamond provides additional support to our view that the observed band at 1205 cm^{-1} is from hexagonal nanodiamond.

Table 4.4 Raman Peaks for SH77#4 (105 minute)

Peak	Width	Area
1205.37	46.5619	342.631
1335.88	8.9011	228.006
1337.22	67.5741	1659.05
1436.55	94.55	1355.01
1538.58	99.316	1725.46

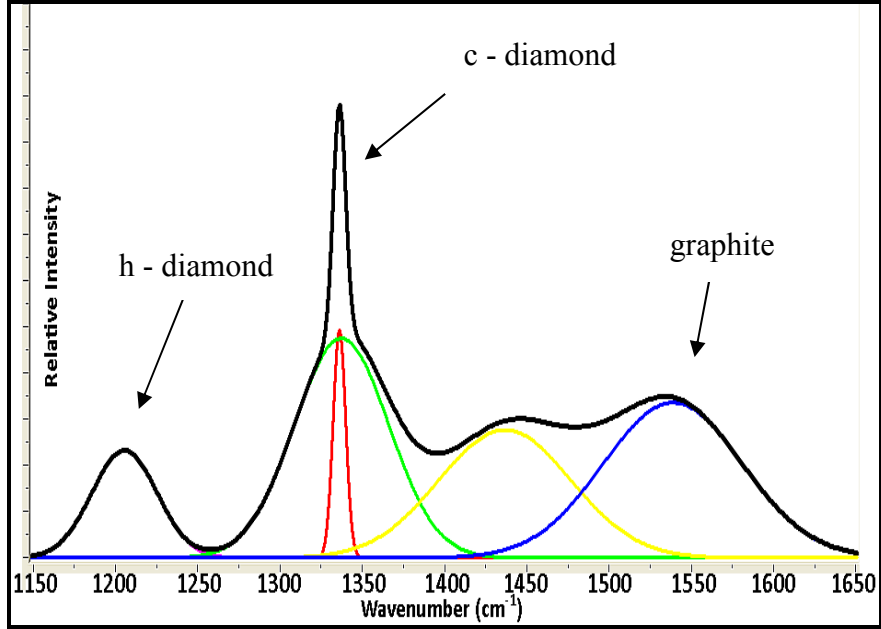


Figure 4.27 Raman Spectrum of Hexagonal Nanodiamonds

4.4 X- Ray Diffraction Results

In order to further look into hexagonal nanodiamonds, we performed XRD measurements on the 105 min sample. XRD was performed on the sample for 4 hrs. and 8 hrs. respectively. The XRD curves obtained by using Cu K_{α} radiation ($\lambda = 1.5418 \text{ \AA}$) are shown in Figure 4.28. The (111) reflections in cubic diamond and (002) reflections in hexagonal diamond appear at $2\theta = 43.934$ and 43.932 degrees respectively. The peak at $2\theta = 44.4$ is believed to originate from hexagonal graphite present in the sample [48]. No clear peaks are observed at $2\theta = 41.37$ and 47.12 which are additional features of hexagonal diamond. It may be so due to a relatively small concentration of hexagonal diamond in our samples.

Table 4.5 Properties of Cubic and Hexagonal Diamond

Property	c - diamond	h - diamond
Structure	cubic	hexagonal
Stacking	ABCABC	ABABAB
Lattice constant (Å)	3.567	a = 2.522; c = 4.119
Band Gap (eV)	5.5	4.5 [25]
XRD peak positions (2θ); planes	43.95 (111)	41.37 (100) 43.95 (111) 47.12 (101)
Corresponding d-spacing (Å) [20]	2.06	2.184 2.06 1.9285

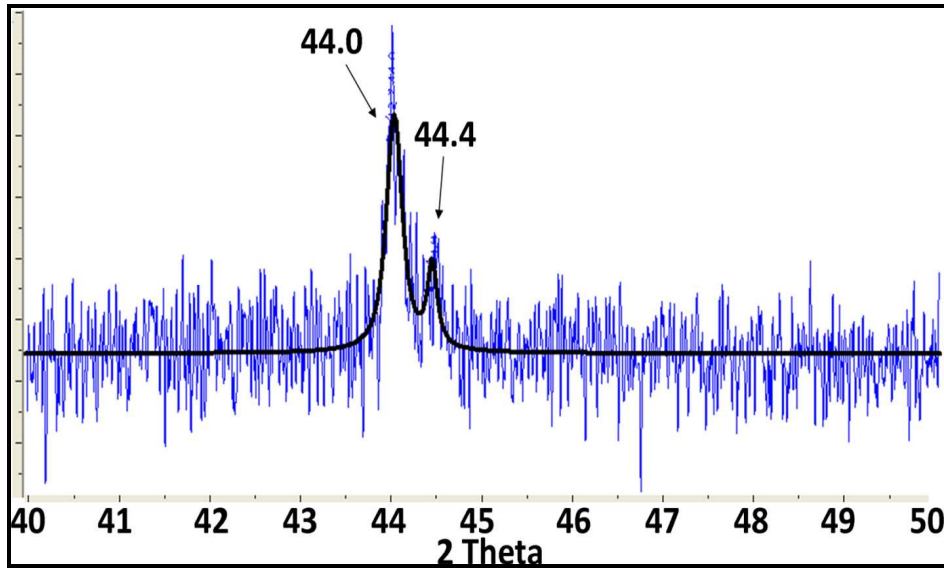


Figure 4.28 XRD Results of SH77#4

CHAPTER 5

CONCLUSIONS

In this dissertation, the techniques of Atomic Force Microscopy, Scanning Electron Microscopy, Raman Spectroscopy and X Ray Diffraction were utilized to study diamond nanoparticles in diamond thin films grown previously by Hot Filament Assisted Chemical Vapor Deposition method. Atomic Force Microscopy was adopted to study the topography and morphology of the diamond thin films. It was observed that the diamond particles appear to be uniformly spread with average height of around 10 nm. The roughness of the surfaces are observed to decrease gradually with the growth period. Scanning Electron Microscopy showed that particle sizes increased with deposition time from very small (~ 10 nm in 15 min sample) to large (~ 200 nm in the 105 min sample). Phonon Confinement Model was beneficial to predict the crystal sizes. Phonon Confinement Model was highly beneficial to study the peak broadening in diamond particles. Further, the occurrence of a peak at 1200 cm^{-1} was attributed to the presence of hexagonal nanodiamonds. X Ray Diffraction was performed on the 105 min sample in order to obtain the microscopic evidence of the presence of hexagonal nanodiamonds. The XRD results showed a major peak at $2\theta = 44$ which may have contributions from both cubic and hexagonal diamond.

APPENDIX

RELATIVE DIAMOND CONCENTRATION CALCULATIONS

Diamond concentration calculations

Scattering cross-section of nondiamond components is 50 times greater than that of diamond [38, 42]

$$\text{Diamond Conc} = \frac{\sum(\text{Diamond components}) \times 50}{[\sum(\text{Diamond components}) \times 50] + \sum(\text{Nondiamond components})}$$

The uncertainty in the value of diamond concentration was calculated by following the standard error – propagation method.

SH76#1 (15mins)

Peak	Width	Area
1220	44.1296	312.267
1333.1	3.7094	504.996
1337.8	74.8238	598.59

$$\begin{aligned} \text{Diamond concentration} &= \frac{(504.996+598.59) \times 50}{[(504.996+598.59) \times 50] + [312.267]} \\ &= 0.99437 \\ &= 99.437\% \pm 5.97\% \end{aligned}$$

SH76 #2 (30mins)

Peak	Width	Area
1257.33	22.929	84.5703
1331.21	19.7901	195.555
1338.15	116.126	1635.81
1449.84	67.2194	424.604
1601.8	22.7182	70.644

$$\begin{aligned} \text{Diamond concentration} &= \frac{(195.555+1635.81) \times 50}{[(195.555+1635.81) \times 50] + [84.5703+424.604+70.644]} \\ &= 0.9937 \end{aligned}$$

$$= 99.37\% \pm 4.6 \%$$

SH76#3 (43mins)

Peak	Width	Area
1330.78	109.109	4911.04
1335.77	34.484	3040.35
1608.15	59.7435	2469.58

$$\begin{aligned} \text{Diamond concentration} &= \frac{(4911.04+3040.35) \times 50}{[(4911.04+3040.35) \times 50] + [2469.58]} \\ &= \frac{397569.5}{400039.08} \\ &= 0.9932 \\ &= 99.32\% \pm 2.2\% \end{aligned}$$

SH77#4 (105mins)

Peak	Width	Area
1210.61	46.5619	328.089
1335.88	8.9011	228.006
1337.22	67.574	1659.05
1436.55	94.5509	1355.01
1538.58	99.3165	1725.46

$$\begin{aligned} \text{Diamond concentration} &= \frac{(228.006+1659.05) \times 50}{[(228.006+1659.05) \times 50] + [328.089+1355.01+1725.46]} \\ &= 0.96513 \\ &= 96.513\% \pm 4.54\% \end{aligned}$$

REFERENCES

1. S. J. Yu, M. W. Kang, H. C. Chang, K. M. Chen, Y. C. Yu; *J. Am. Chem.Soc* **2005**,*127*, 17604
2. L. C. L. Huang, H. C. Chang; *Langmuir* **2004**, *20*, 5879
3. K. Iakoubovskii, K. Mitsuishi and K. Furuya; *Nanotechnology* **2008**, *19*, 155705 (5pp)
4. Eiji Osawa, NANONET INTERVIEW, Opening up a new world of nanodiamonds, dispersing nanodiamonds (Issued in Japanese: March 8, **2006**)
5. R. D. McKeag and R.B. Jackman; *Diamond Relat. Mater* **7** **1998**, pp. 513–518
6. C. A. Dark; Deposition and characterization of diamond films, MS Thesis, University of Texas at Arlington, **1990**
7. R. C. Hyer; A study of defects in diamond films grown by chemical vapor deposition, PhD Thesis, University of Texas at Arlington,**1993**
8. A.R. Ubbelohde and F.A. Lewis; *Graphite and its crystal compounds*, Oxford University Press, London, **1960**, p.7
9. www.diamonds.gl
10. invsee.asu.edu/nmodules/carbonmod/bonding.html
11. Status and Applications of Diamond and Diamond-Like materials; An emerging Technology, Report of the committee on superhard materials; National Academy press, **1990**
12. X. K. Zhang, J. G. Guo and Y. F. Yao; *Phys.Stat.Sol (a)* **133**,377 **1992**
13. A. Masood, M. Aslam, M. A. Tamor and T. J. Potter; *Appl.Phys.Lett* **61**,**1992** **1832**
14. A.T. Collins; *The Optical and Electronic Properties of Semiconductor*, **1993**
15. K. Iakoubovskii and G. J. Adriaenssens; Luminescence excitation spectra in diamond *Phys. Rev. B* **61** (**2000**) 10174
16. http://en.wikipedia.org/wiki/Crystallographic_defects_in_diamond

17. J. P. Goss et al; Phys. Rev. B 67 (2003) 165208
18. J.H. Chen et al.; "Voidites in polycrystalline natural diamond" Phil. Mag. Lett 77 (1988) 135
19. I. Kiflawi et al.; "'Natural' and 'man-made' platelets in type-Ia diamonds" Phil. Mag. B 78 (1998) 299
20. F.P.Bundy and J.S.Kasper; J. Chem. Phys 46 4737 (1967)
21. http://www.geocities.jp/ohba_lab_ob_page/structure4.html
22. K. Lonsdale; Nature (London) 153, 669 (1944).
23. <http://www.mindat.org/min-2431.html>
24. Pan, Zicheng; Sun, Hong; Zhang, Yi; and Chen, Changfeng (2009). "Harder than Diamond: Superior Indentation Strength of Wurtzite BN and Lonsdaleite". *Physical Review Letters* **102** (102): 055503.
25. Salehpour M R, Satpathy S, Physical Review B, 41, (1990), 3048
26. <http://cst-www.nrl.navy.mil/lattice/struk/hexdia.html>
27. K lakoubovskii, KMitsubishi and K Furuya, Nanotechnology 19 (2008) 155705 (5pp)
28. http://www.nanoworld.com/probes_catalog.html
29. www.veeco.com, Probes catalog
30. http://en.wikipedia.org/wiki/Raman_scattering
31. Raman Scattering Theory- David W. Hahn, Department of Mechanical Aerospace Engineering, University of Florida
32. R. C. Hyer; A study of defects in diamond films grown by chemical vapor deposition, PhD Thesis, University of Texas at Arlington, 1993
33. W.Hayes and R.Louden, Scattering of Light by crystals, John Wiley and sons, New York (1978).
34. www.horiba.com
35. Rajarshi Chakraborty, Suresh C Sharma, J Kyle LaRoque, 2010, Journal of Nano Research, 12, 123

36. R.C. Hyer, M.Green,K.K. Mishra and S.C.Sharma,; Journal of Materials Science Letters, 10, 515-518,(1991)
37. R.C. Hyer, M. Green and S.C.Sharma, Phys. Rev. B 49, 14573-14581 (1994)
38. S. C. Sharma, M.Green, R.C.Hyer, C.A.Dark, T.D. Black, A.R.Chourasia, D.R.Chopra and K.K.Mishra, Growth of Diamond Films and Characterization by Raman, Scanning Electron Microscopy and X-Ray Photoelectron-Spectroscopy, Journal of Materials Research, 5,2424-2431, (1990)
39. D.S.Knight and W.B.White, Characterization of Diamond Films by Raman-Spectroscopy, Journal of Materials Research, 4, 385-393, (1989).
40. R.J.Nemanich, S.A. Solin and R.M.Martian, Phys. Rev. B 23, 6348 (1981)
41. R. J. Nemanich, S.A. Solin, Phys. Rev. B 20, 392(1979)
42. Zhu XD, Xu YH, Naramoto H, Narumi K, Miyashita A, Miyashita K,(2003) J Phys- Condens Mat 15: 2899
43. H. Richter, Z. P. Wang, and L. Ley, Solid State Commun. **39**, 625 _1981
44. M. Yoshikawa, Y. Mori, M. Maegawa, G. Katagiri, H. Ishida and A. Ishitani, Appl. Phys. Lett. **62**, 3114 _1993
45. Nemanich RJ, Glass JT, Lucovsky G, Shroder RE (1998), J Vac Sci Technol A 6:1783
46. Ager JW, Veirs DK, Rosenblatt GM (1991), Physical Review B, 43:6491
47. Wu BR, Xu J (1998) Physical Review B, 57:13355
48. Amornkitbamrung V, Burinprakhone I, Jarernboon W, Surf Coat Tech (2009), 203: 1645

BIOGRAPHICAL INFORMATION

The author completed his undergraduate degree in Electrical Engineering from West Bengal University of Technology, Kolkata, India. His undergraduate project was on “LARGE SCALE SYNTHESIS AND OPTICAL PROPERTIES OF ZnO NANOSTRUCTURES” from Saha Institute of Nuclear Physics, Kolkata, India. His current research interests are directed at developing and understanding the optical properties of semiconductors. He has authored two papers in scientific journals and presented papers at national conferences under the mentorship of Prof. Suresh C Sharma. He intends to continue his research activities in academia and is seeking an opportunity to pursue his doctoral studies